



STAT1 promotes ferroptosis and inflammation in mouse hepatic ischemia-reperfusion injury



Kun Wu , Ting Xu , Baofei Jiang , Xiangyou Yu , Yi Wang , Hu Sun , Zuyi Zhao , Meiting Du , Shaochuang Wang , & Long Ma

Hepatic ischemia reperfusion injury (HIRI) is a critical complication in liver surgery and transplantation, driven by excessive inflammation and hepatocellular death. Although ferroptosis is recognized as a major form of regulated cell death in HIRI, the upstream regulators of this process remain poorly defined. Here, we show that the transcription factor STAT1 plays a pivotal role in promoting ferroptosis and inflammation during HIRI. Using male mice subjected to partial hepatic ischemia followed by reperfusion, we find that STAT1 protein is significantly upregulated in liver tissues. Genetic deletion of *Stat1* markedly reduces lipid peroxidation, suppresses proinflammatory cytokine expression, and improves liver histology and function. Mechanistically, STAT1 represses miR-497-5p transcription, leading to HDAC7 activation, which together promotes ferroptosis and inflammatory responses in HIRI. These results identify STAT1 as a central link between ferroptosis and inflammation in HIRI, suggesting that targeting STAT1 may offer a novel therapeutic strategy for liver protection in clinical settings.

Hepatic ischemia-reperfusion injury (HIRI) is a common and complex pathological process during liver surgery^{1–3}. Reperfusion of the liver after ischemia results in a series of irreversible damages, such as oxidative stress, inflammatory response, and cell apoptosis, severely impacting the survival rate and health condition of surgical patients^{4,5}. Epidemiological data shows that HIRI is a common complication in liver transplantation, liver resection, and coronary artery bypass surgery^{6–8}. Therefore, a comprehensive study of the pathogenesis of HIRI and the discovery of potential therapeutic targets and strategies are of significant clinical importance for improving the prognosis of surgical patients.

Recent studies have indicated that signal transducer and activator of transcription 1 (*Stat1*) plays a crucial role in HIRI^{9–11}. STAT1 is a transcription factor involved in the regulation of cell immune response and inflammation processes^{12,13}. In HIRI, the expression level of *Stat1* is elevated and interacts with multiple signal pathways associated with ferroptosis and inflammatory response¹⁴. Furthermore, the non-coding small RNA, *miR-497-5p*, is considered to have potential regulatory roles in HIRI^{15–18}. The promoter region of *miR-497-5p* is significantly enriched under the

regulation of *Stat1*, which suppresses the expression level of *miR-497-5p*¹⁹. However, further research and validation are needed to elucidate the exact mechanisms of *Stat1* and *miR-497-5p* in HIRI¹⁹.

To investigate the role of *Stat1* in HIRI, we established a mouse model of HIRI and extracted RNA from the liver of both model and control mice for RNA-seq sequencing and differential gene enrichment analysis. Additionally, we used proteomics analysis techniques to identify and enrich proteins in the mouse liver, thereby further selecting core factors. Moreover, an in vitro hypoxia/reoxygenation (H/R) cell model was established in the human liver cell line MIHA, and various biochemical and molecular biology techniques, such as hematoxylin and eosin (H&E) staining, Western blot, RT-qPCR, and immunofluorescence staining, were applied to detect changes in cellular functional damage, inflammation state, oxidative stress, and ferroptosis.

Through transcriptome sequencing and proteomics analysis, we identified *Stat1* as a key regulatory factor in HIRI. We found that the expression level of *Stat1* significantly increases in HIRI and interacts with multiple signal pathways associated with ferroptosis and inflammatory

¹Department of Gastrointestinal Surgery, The Affiliated Huai'an No.1 People's Hospital of Nanjing Medical University, Huai'an, 223300, P.R. China. ²Hematology Research Laboratory, The Affiliated Huai'an No.1 People's Hospital of Nanjing Medical University, Huai'an, 223300, P.R. China. ³Department of Gastrointestinal Surgery, Shanghai Tenth People's Hospital, Shanghai, P.R. China. ⁴Department of Critical Care Medicine, The First Affiliated Hospital of Xinjiang Medical University, Urumqi, 830054, P.R. China. ⁵Department of Respiratory and Critical Care Medicine, The First Affiliated Hospital of Xinjiang Medical University, Urumqi, 830054, P.R. China. ⁶Department of Hepatobiliary Surgery, The Affiliated Huai'an No.1 People's Hospital of Nanjing Medical University, Huai'an, 223300, P.R. China. ⁷These authors contributed equally: Kun Wu, Ting Xu, Baofei Jiang. e-mail: dr_wukun@163.com; malong8617@163.com

response. Further research revealed that knockdown of *Stat1* enhances cell viability and mitigates cell apoptosis and inflammatory response in the H/R cell model. Additionally, *Stat1* affects cell proliferation, apoptosis, ferropotosis, and inflammatory response by regulating the expression of *miR-497-5p* and Histone Deacetylase 7 (*HDAC7*)¹⁴. The impact of *Stat1* on *miR-497-5p* and *HDAC7* in HIRI was also validated in vivo mouse experiments²⁰⁻²².

Our study elucidates a mechanistic role for *STAT1* in HIRI, whereby it regulates ferropotosis and the inflammatory response by suppressing the non-coding RNA *miR-497-5p* and activating its downstream target *HDAC7*. Our findings, supported by transcriptome sequencing, proteomics analysis, and in vitro and in vivo experiments, confirm the regulation of *Stat1* on *miR-497-5p* and *HDAC7*, thereby influencing cell proliferation, apoptosis, ferropotosis, and inflammatory response. These findings contribute to a deeper understanding of the pathogenesis of HIRI and provide new targets and strategies for clinical treatment, ultimately improving the prognosis of surgical patients.

Results

Molecular mechanisms and key gene regulation in HIRI

HIRI is a major factor affecting the success rate of liver resection and transplantation procedures. The pathophysiological processes and mechanisms underlying HIRI are complex, involving both the damage caused during liver ischemia and the subsequent damage during liver reperfusion²³. The aim of this study is to explore the molecular mechanisms involved in the treatment or prevention of HIRI.

To establish the HIRI mouse model, we performed occlusion of the portal vein and hepatic artery in mice for 1 h, followed by releasing the occlusion. The Sham group consisted of mice without vascular occlusion (Supplementary Fig. 1A). Macroscopic examination of the HIRI group showed obvious lobular blockage, indicating successful occlusion. With reperfusion, the ischemic liver gradually regained its normal red color (Supplementary Fig. 1B). H&E staining revealed hepatocyte death, sinusoidal congestion, and vacuolation in the HIRI group, indicating liver tissue damage (Supplementary Fig. 1C). Transmission electron microscopy (TEM) images showed that hepatocytes in the Sham group had normal structure, regular nuclear shape, evenly distributed chromatin, and normal mitochondrial structure, while hepatocytes in the HIRI group had unclear structure, thickened nuclear membrane, and numerous high-density circular inclusions containing necrotic mitochondria (Supplementary Fig. 1D). Peripheral blood collected from the mice revealed significantly elevated levels of alanine aminotransferase (ALT), aspartate aminotransferase (AST), and inflammatory factors interleukin-1 β (IL-1 β) and interleukin-6 (IL-6) in the HIRI group compared to the Sham group (Supplementary Fig. 1E-H), confirming the successful construction of the HIRI mouse model.

To investigate the molecular mechanisms directly associated with HIRI further, we performed transcriptome sequencing analysis on liver samples from 15 HIRI and Sham mice (Fig. 1A). Firstly, we normalized the microarray data using standardization methods, and PCA analysis confirmed the successful elimination of batch effects (Fig. 1B, C). Differential gene analysis revealed 238 significant differentially expressed genes (DEGs) between the HIRI and control groups, with 181 upregulated and 57 downregulated (Fig. 1D). Heat maps were generated to visualize the top 100 upregulated and downregulated genes based on the degree of differential expression (Fig. 1E).

Gene ontology (GO) enrichment analysis indicated that these genes are mainly involved in biological processes such as cellular stress, I-kappaB kinase/NF-kB signaling, protein interactions, autophagy, and regulation of cell number homeostasis. They are related to cellular structures such as autophagosomes, nuclear pore complexes, and nuclear envelopes, as well as molecular interactions involving cell signaling receptors, molecular chaperones, protein heterodimerization, protein phosphatase binding, and chemokine receptor binding (Fig. 1F, Supplementary Table 1). Kyoto Encyclopedia of Genes and Genomes (KEGG) pathway analysis further confirmed the importance of DEGs in signaling pathways such as

inflammation, cell survival, autophagy, JAK-STAT, NF-kB, and fatty acid biosynthesis (Fig. 1G).

To delve deeper into the key cellular mechanisms and disease processes underlying HIRI, we quantified 171 biological processes using the GSVA method (Fig. 1H), identifying 12 significantly altered biological pathways in HIRI (Fig. 1I, J). We observed upregulated pathways associated with glioblastoma, prostate cancer, and myocardial contraction in relation to HIRI (Fig. 1K). In terms of cell signaling and regulation, we found enhanced autophagy and hedgehog signaling pathways, as well as decreased phosphatidylinositol signaling system activity (Fig. 1L). In metabolic pathways, there was an increase in amino sugar and nucleotide sugar metabolism, cytochrome P450-mediated xenobiotic metabolism, and drug metabolism capacity (Fig. 1M). Lastly, in pathways related to cellular composition and function, there was an increase in interactions involving neuroactive ligand-receptor pairs, while activities in the glycolipid biosynthesis pathway and cytoplasmic DNA sensing pathway were reduced (Fig. 1N).

In conclusion, the pathological mechanisms of HIRI involve key biological processes related to disease-associated signaling, cellular regulation, metabolic pathways, and cellular functions. These findings provide valuable insights and a foundation for further research and intervention strategies for HIRI.

In order to identify the key genes involved in the pathogenesis of HIRI, we employed a combination of Weighted Gene Co-expression Network Analysis (WGCNA) analysis and the Lasso regression algorithm (Supplementary Fig. 2A). First, we performed clustering on 15 normal samples and 15 HIRI samples, removing obvious outliers by setting a threshold (Supplementary Fig. 3A). Setting the soft threshold to 6, the scale independence curve flattened, and the average connectivity was high, indicating suitability for subsequent analysis (Supplementary Fig. 3B, C). Based on the dissimilarity matrix, hierarchical clustering was performed on the genes in the HIRI dataset, resulting in a dendrogram (Supplementary Fig. 2B). After merging strongly correlated modules with a clustering height threshold of 0.25, we identified 9 gene modules for further investigation (Supplementary Fig. 2C). To screen for modules highly associated with HIRI, we performed principal component analysis (PCA) on the genes within each module and extracted the value of the first principal component as the module eigengene (ME). Subsequently, we determined the clinical significance of the modules by assessing the correlation between the ME values and clinical features. The results indicated a strong positive correlation between the Brown module and HIRI ($r = 0.73, p = 5e - 06$), and it exhibited the highest gene importance (Supplementary Fig. 2D, Supplementary Fig. 3D). The correlation analysis of each module with HIRI is shown in Supplementary Fig. 3E-M. Therefore, the Brown module was selected for further analysis.

To further explore the characteristic genes regulating HIRI, we overlapped the key module genes from WGCNA analysis and the DEGs identified by differential analysis, resulting in 94 overlapping genes (Supplementary Fig. 2E). By using the Lasso regression algorithm, a machine learning technique, we further screened the overlapping genes by selecting the lambda parameter that yielded the smallest error based on cross-validation, resulting in the identification of 3 key genes (Supplementary Fig. 2F). Comparing the HIRI group with the normal group, we observed a significant increase in the expression level of the gene *Stat1*, while *Gpx4* and *Fbxw13* showed significant decreases (Supplementary Fig. 2G). The diagnostic capability of the characteristic genes was further validated by the receiver operating characteristic (ROC) curve analysis (Supplementary Fig. 2H-J).

These results suggest that the genes *Stat1*, *Gpx4*, and *Fbxw13* play a central role in the occurrence and development of HIRI, and they exhibit strong diagnostic and predictive abilities.

Proteomic analysis reveals DEPs and their functions in the HIRI process

We first extracted total proteins from the livers of mice in the HIRI group and the Sham group, followed by liquid chromatography-tandem mass spectrometry analysis (Fig. 2A). Normalization treatment and PCA PCA of

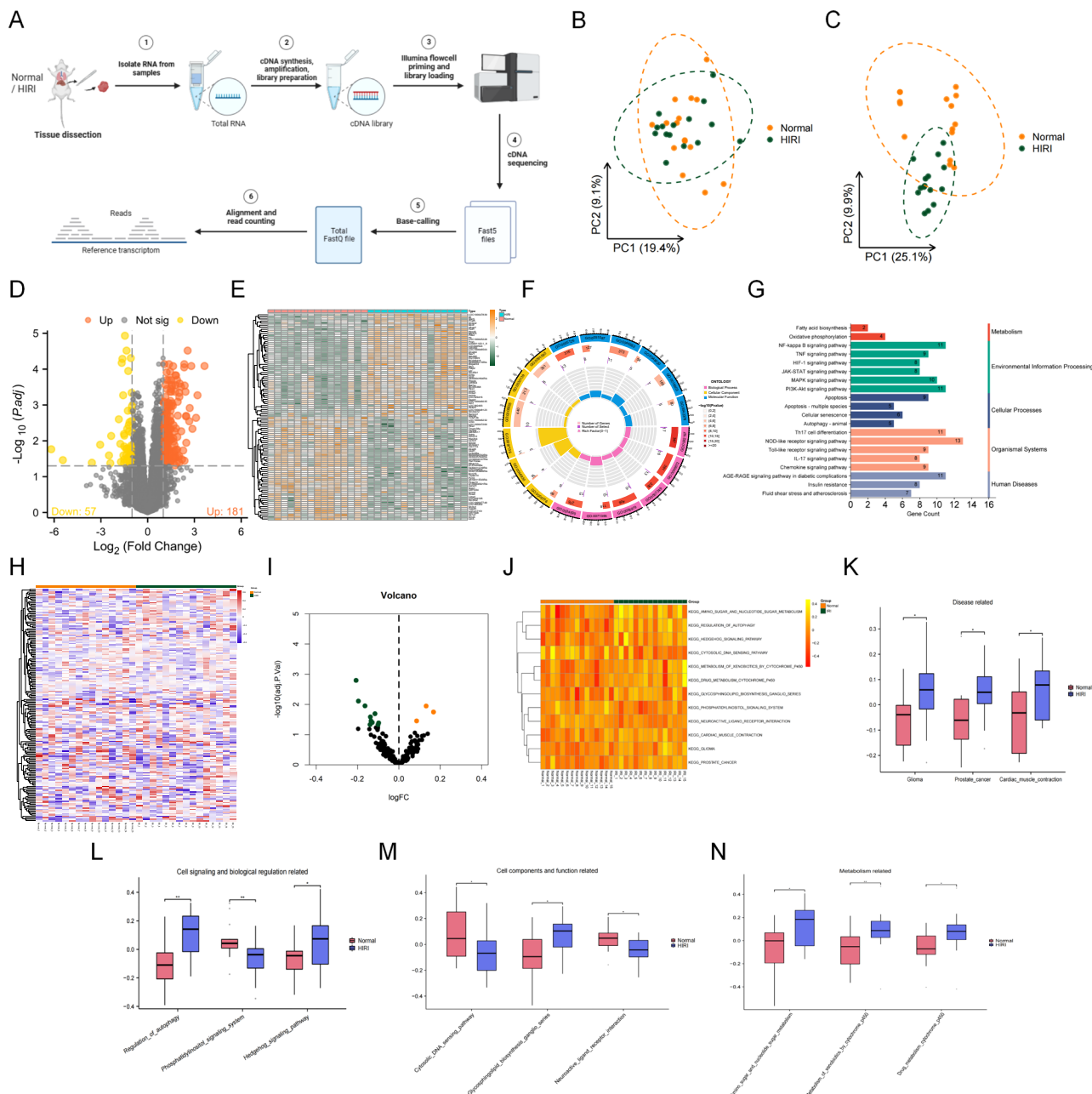


Fig. 1 | Differential Transcriptome analysis and functional enrichment of the normal and HIRI groups. (A) Schematic diagram of the transcriptome sequencing workflow (Created by BioRender); (B, C) PCA analysis of normal and HIRI samples (Sham = 15, HIRI = 15), where the x and y axes represent the two principal components before and after PCA, respectively, with the proportion of explained variance in parentheses; (D) Volcano plot showing the differential expression of 238 DEGs between normal and HIRI samples, with orange representing significantly upregulated genes, yellow dots representing significantly downregulated genes, and gray dots representing genes with no expression difference; (E) Heatmap displaying the top 50 significantly upregulated and downregulated genes, with orange indicating high expression and green indicating low expression; (F) Circular plot illustrating the GO functional enrichment analysis of DEGs, with outer to inner layers representing functional categories, the total number of genes within each category, the number of significantly upregulated genes, and the enrichment factor;

(G) Enrichment analysis of DEGs in KEGG pathways, listing the number of genes enriched in each pathway and organizing them into the top six categories of KEGG Pathway; (H) GSVA analysis depicting a heatmap of 171 metabolic pathways in normal and HIRI samples (Sham = 15, HIRI = 15), with red indicating enhanced pathways and blue indicating suppressed pathways; (I, J) Volcano plot and heatmap showing the differential expression of metabolic pathways, with orange indicating significant enhancement and green indicating significant suppression in the volcano plot, and yellow and red indicating significant enhancement and suppression, respectively, in the heatmap; (K–N) Boxplots illustrating the differential feature scores of disease-related pathways, cell signaling and regulation-related pathways, metabolism-related pathways, and cell composition and function-related pathways. The comparison between the two groups is indicated as $*P < 0.05$, $**P < 0.01$, and $***P < 0.001$.

the data indicated a clear separation in protein expression patterns between the HIRI and control groups, demonstrating significant differences between the experimental and Sham groups (Fig. 2B, C). The analysis of mass spectrometry data revealed 287 significant DEPs between the

HIRI and Sham groups, with 130 upregulated and 157 downregulated proteins (Fig. 2D). A heatmap of the top 100 upregulated and downregulated proteins was plotted based on the degree of differential expression (Fig. 2E).

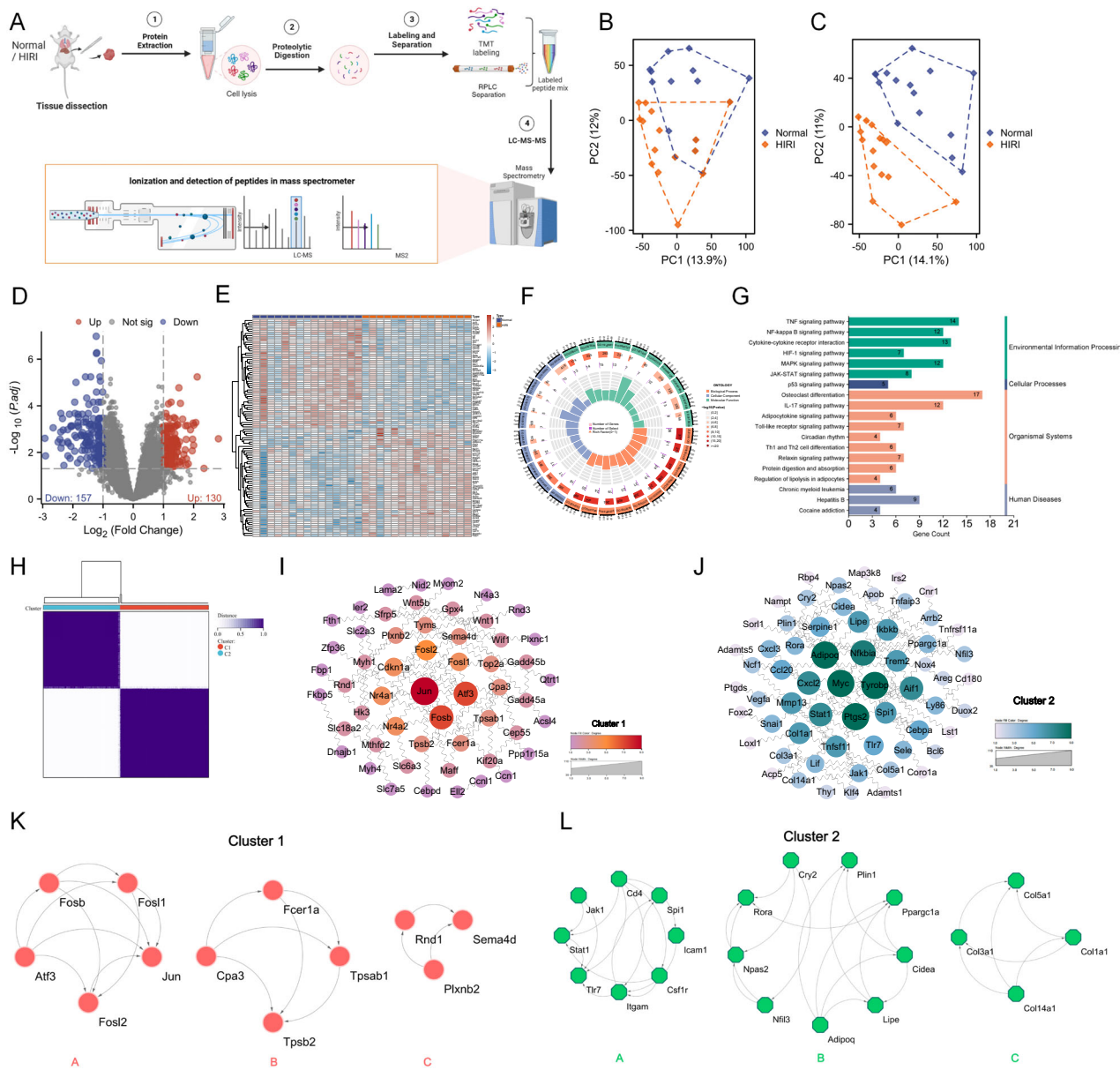


Fig. 2 | Differential proteome analysis and functional enrichment of the normal and HIRI groups. (A) Schematic diagram of the proteomics analysis workflow (Created by BioRender); (B, C) PCA analysis of normal and HIRI samples (Sham = 15, HIRI = 15), with the x and y axes representing the two principal components before and after PCA, respectively, and the proportion of explained variance in parentheses; (D) Volcano plot showing the differential expression of 287 DEPs between Sham and HIRI samples, with red dots representing significantly upregulated proteins, blue dots representing significantly downregulated proteins, and gray dots representing proteins with no expression difference; (E) Heatmap displaying the top 50 significantly upregulated and downregulated proteins, with red indicating high expression and blue indicating low expression; (F) Circular plot illustrating the

GO functional enrichment analysis of DEPs, with outer to inner layers representing functional categories, the total number of proteins within each category, the number of significantly upregulated proteins, and the enrichment factor; (G) Enrichment analysis of DEPs in KEGG pathways, listing the number of proteins enriched in each pathway and organizing them into the top six categories of KEGG Pathway; (H) Cluster analysis heat map when $k = 2$; (I, L) PPI network graphs of cluster 1 ($n = 154$) and cluster 2 ($n = 133$) constructed using the STRING database, where nodes represent proteins and edges represent relationships between proteins, with the color depth and size of the nodes determined by protein degree values; (K, J) Top three protein clusters identified by MCODE in Cytoscape software for each protein cluster in the PPI network.

GO enrichment analysis showed that these DEPs are mainly involved in regulating biological processes such as inflammatory response, muscle cell proliferation, regulation of small molecule metabolic processes, and cell chemotaxis. They are primarily located in key cellular regions such as collagen-containing extracellular matrix, RNA polymerase II transcription regulation complex, and immune synapse, exhibiting cytokine activity and possessing the ability to bind specifically to DNA transcription factors

associated with RNA polymerase II (Fig. 2F, Supplementary Table 2). KEGG pathway analysis demonstrated significant enrichment of DEPs in several critical signaling pathways, including the JAK-STAT signaling pathway, TNF signaling pathway, IL-17 signaling pathway, NF- κ B signaling pathway, and HIF-1 signaling pathway (Fig. 2G).

Consensus clustering analysis and Protein–Protein Interaction (PPI) network construction were performed on the 287 DEPs (Supplementary

Fig. 4A) to explore potential protein expression patterns and molecular subtypes. The consistency of clustering results under different cluster numbers (k values) was evaluated using the comprehensive CDF curve (Supplementary Fig. 4B), and the stability of clustering results was quantified by the area under the CDF curve (Supplementary Fig. 4C). Finally, the DEPs were divided into two protein subtypes: cluster 1 ($n = 154$) and cluster 2 ($n = 133$) (Fig. 2H). The effectiveness of this classification was further confirmed by average within-cluster consistency evaluation (Supplementary Fig. 4D).

A PPI network, revealing the complex interrelationships among these proteins, was constructed using a confidence threshold of >0.7 (Supplementary Fig. 4E). Cytoscape software was used to process the PPI networks of the two protein subtypes, and the proteins were sorted based on their degree values, with the results presented in Fig. 2I, J, respectively. Through topological analysis, key protein clusters were identified in the networks. In cluster 1, the top three protein clusters with the highest MCODE algorithm scores were closely associated with inflammation, cell signaling pathways, and cellular survival key pathways (Fig. 2K, L, Supplementary Fig. 4F). In cluster 2, the top three protein clusters with the highest MCODE scores were respectively associated with the JAK-STAT signaling pathway, AMPK signaling pathway, and inflammation and metabolic processes (Fig. 2L, Supplementary Fig. 4G).

To identify the proteins playing a crucial role in the HIRI process, Venn diagram analysis was performed on the top 15 proteins with the highest degree values and the top-ranked protein clusters by the MCODE algorithm, resulting in the identification of seven core proteins (Supplementary Fig. 4H, I). Compared to the Sham group, the expression levels of Spi1 and STAT1 proteins were significantly increased in the HIRI group, while Jun, Atf3, Fosb, Fosl2, and Fosl1 were significantly decreased (Supplementary Fig. 4J). ROC curve analysis further validated the potential of these proteins as HIRI biomarkers (Supplementary Fig. 4K).

In conclusion, the proteins Jun, Atf3, Fosb, Fosl2, Fosl1, Spi1, and Stat3 are involved in regulating key biological processes such as inflammatory response, cell signaling, cellular survival, and metabolic processes in HIRI. They also hold potential as biomarkers for HIRI.

To identify potential therapeutic targets for HIRI, we conducted a combined analysis of transcriptomics and proteomics. Our results showed that *Stat1* plays a critical role in both the transcriptional and protein levels in the HIRI group compared to the Sham group, with increased expression levels of both protein and mRNA (Supplementary Fig. 5A). STAT1 is an important transcription factor that, once activated, induces the expression of various inflammatory factors. It promotes cell proliferation and migration and has pro-apoptotic and pro-inflammatory effects^{24,25}. To further understand the molecular mechanisms of STAT1 in mouse models and human diseases, we performed network analysis using the GeneMINA database for both the *Stat1* gene in mice and the *STAT1* gene in humans (Supplementary Fig. 5B, C). Functional enrichment analysis revealed STAT1's involvement in the regulation of autophagy, primary miRNA binding, histone acetyltransferase binding, regulation of apoptosis signaling pathways, and immune response modulation, among other biological processes. Moreover, the analysis demonstrated the consistency of STAT1's function in mice and humans (Supplementary Fig. 5D, E). Hence, *STAT1* not only plays a pivotal role in understanding the pathophysiology of HIRI but also represents a potential novel approach for treating this disease.

Upregulation of *Stat1* and its regulatory role in hepatocellular injury in HIRI and H/R models

To further validate the potential role of *Stat1* in HIRI identified in the previous bioinformatics analysis, protein and mRNA expression levels of STAT1 were significantly upregulated in HIRI as determined by real-time quantitative polymerase chain reaction (RT-qPCR) and Western blot techniques (Fig. 3A, B). Immunofluorescence staining of liver tissue sections revealed a significant increase in colocalization of STAT1 and the hepatocyte marker HNF4 (Fig. 3C), suggesting that the upregulation of STAT1 may be involved in the process of HIRI.

Hepatocellular apoptosis and inflammatory response are crucial events in HIRI and represent important areas of study²⁶. To investigate the functional role of STAT1 in the process of hepatocellular H/R injury, we constructed in vitro H/R models by subjecting MIHA and AML12 hepatocytes to 24 h of hypoxia followed by 18 h of reoxygenation (Supplementary Fig. 6A). Optic microscopy observation of cell morphology revealed clear signs of cell death, including membrane rupture and foaming, in the H/R-treated group compared to the normal control cells (Supplementary Fig. 6B). CCK-8 assay and flow cytometry were used to assess cell viability and apoptosis under different conditions, and the results demonstrated a significant decrease in cell viability and an increase in apoptosis rate after H/R treatment (Supplementary Fig. 6C, D). Western blot analysis further confirmed the increased expression of apoptotic markers Bax and cleaved Caspase-3 and decreased expression of Bcl-2 in the H/R group (Supplementary Fig. 6E, Supplementary Fig. 7C). Additionally, STAT1 expression was significantly upregulated in H/R-treated cells, as confirmed by RT-qPCR and Western blot (Supplementary Fig. 6F, G, Supplementary Fig. 7A, B).

To further explore the regulatory role of *Stat1* in H/R, sh-*Stat1*#1/2 was used to knock down *Stat1* in MIHA cells and AML12 cells (Supplementary Fig. 6A), and the knockdown efficiency was validated by RT-qPCR (Supplementary Fig. 8A). The CCK-8 assay results showed increased cell viability in H/R cells after STAT1 knockdown (Fig. 3D). Flow cytometry and TUNEL staining revealed that STAT1 knockdown alleviated cell apoptosis (Fig. 3E, F, Supplementary Fig. 7D) and significantly reduced the expression levels of Bax and cleaved caspase-3 while increasing the expression of Bcl-2 (Fig. 3G, H, Supplementary Fig. 7E). Furthermore, the knockdown of STAT1 also led to a decrease in the inflammatory factors IL-1 β and IL-6 (Fig. 3I, J, Supplementary Fig. 7F, G).

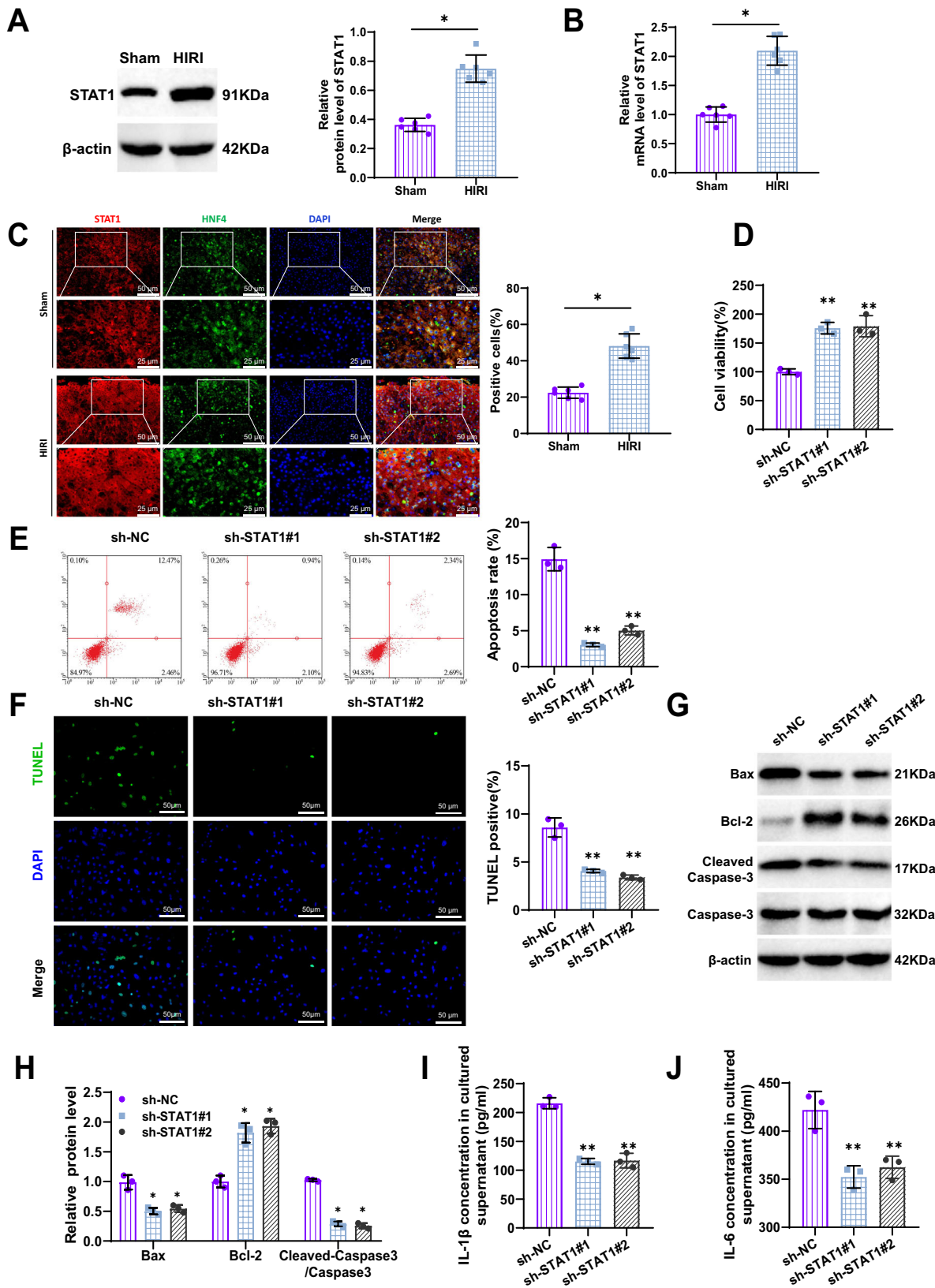
In conclusion, both in the HIRI and H/R models, *Stat1* expression was significantly upregulated, and the knockdown of *Stat1* effectively reversed H/R-induced hepatocellular injury by promoting cell viability, reducing apoptosis rate, and suppressing the expression of apoptosis-related proteins. These findings highlight *Stat1* as a potential therapeutic target that could alleviate HIRI-induced damage and improve liver function.

Stat1 regulates HIRI by modulating the activity of the miR-497-5p promoter

The interaction between STAT transcription factors and various miRNAs plays a crucial role in regulating the homeostasis, differentiation, and function of immune cells. Specifically, miRNAs, a group of non-coding endogenous RNA molecules, exert specific functional roles in disease progression by regulating gene expression^{27,28}. In this context, changes in the expression of miR-497-5p are believed to significantly impact the extent of HIRI^{29,30}. Therefore, we postulate that STAT1, miR-497-5p, and their associated target genes may form a complex gene regulatory network in HIRI and play important roles in the HIRI process.

Previous studies have shown that STAT1 translocates from the cytoplasm to the nucleus upon activation, where it serves as a transcription factor regulating the expression of various genes^{31,32}. Silico analysis using the JASPAR database predicted the presence of multiple transcription binding sites between STAT1 and the miR-497-5p promoter region (Fig. 4A, B). Evidence of STAT1 regulation of miR-497-5p was also found in the TransmiR database (Supplementary Fig. 9A, B).

To investigate the regulatory relationship between STAT1 and miR-497-5p in HIRI further, we examined the expression of miR-497-5p using RT-qPCR in a mouse HIRI model and an H/R cell model. The results showed a significant decrease in miR-497-5p expression was significantly downregulated in the HIRI models compared with controls (Supplementary Fig. 9C, D). Additionally, there was a significant negative correlation between the expression of STAT1 and miR-497-5p (Supplementary Fig. 9E). In HEK-293T cells, we performed a ChIP experiment to assess the enrichment of STAT1 at the miR-497-5p promoter region, and the results demonstrated a substantial enrichment of STAT1 at the miR-497-5p promoter region (Fig. 4C). Fluorescent luciferase reporter gene assays with mutated binding sites revealed that overexpression of STAT1 significantly



reduced the luciferase activity of the wild-type pGL3-*miR-497-5p* promoter but had no effect on the luciferase activity of the mutated type pGL3-*miR-497-5p* promoter (Fig. 4D–F). These results indicate that STAT1 can decrease the activity of the *miR-497-5p* promoter.

Furthermore, silencing or overexpression experiments of *Stat1* in HEK-293T cells demonstrated that *miR-497-5p* expression was significantly increased in the sh-*Stat1* group compared to the sh-NC group, while *miR-497-5p* expression was significantly decreased in the oe-*Stat1* group

Fig. 3 | Regulatory role of *Stat1* in HIRI and H/R models. (A-B) Expression of STAT1 in the Sham group and HIRI mice group (Normal: $n = 6$, HIRI: $n = 6$) was detected by Western blot (A) and RT-qPCR (B); (C) Co-expression of STAT1 (red) and hepatocyte marker HNF4 (green) in liver slices of the Sham group and HIRI mice group was detected by immunofluorescence staining and corresponding statistical graphs were provided, with nuclei stained with DAPI (blue); (D) Cell viability of H/R cells with reduced STAT1 was detected by CCK-8 assay; (E) Cell apoptosis rate was detected by flow cytometry and corresponding statistical graphs were

provided; (F) Cell apoptosis was detected by TUNEL fluorescence staining, and corresponding statistical graphs were provided (scale bar: 50 μ m); (G-H) Protein expression levels of apoptotic markers Bax, Bcl-2, cleaved Caspase-3, and Caspase3 in cells were detected by Western blot; (I-J) Expression levels of inflammatory factors IL-1 β and IL-6 in cells with reduced STAT1 were detected by ELISA. Data are presented as mean \pm standard deviation. All cell experiments were repeated three times. Comparison between the two groups was analyzed using * $P < 0.05$, ** denotes $P < 0.01$.

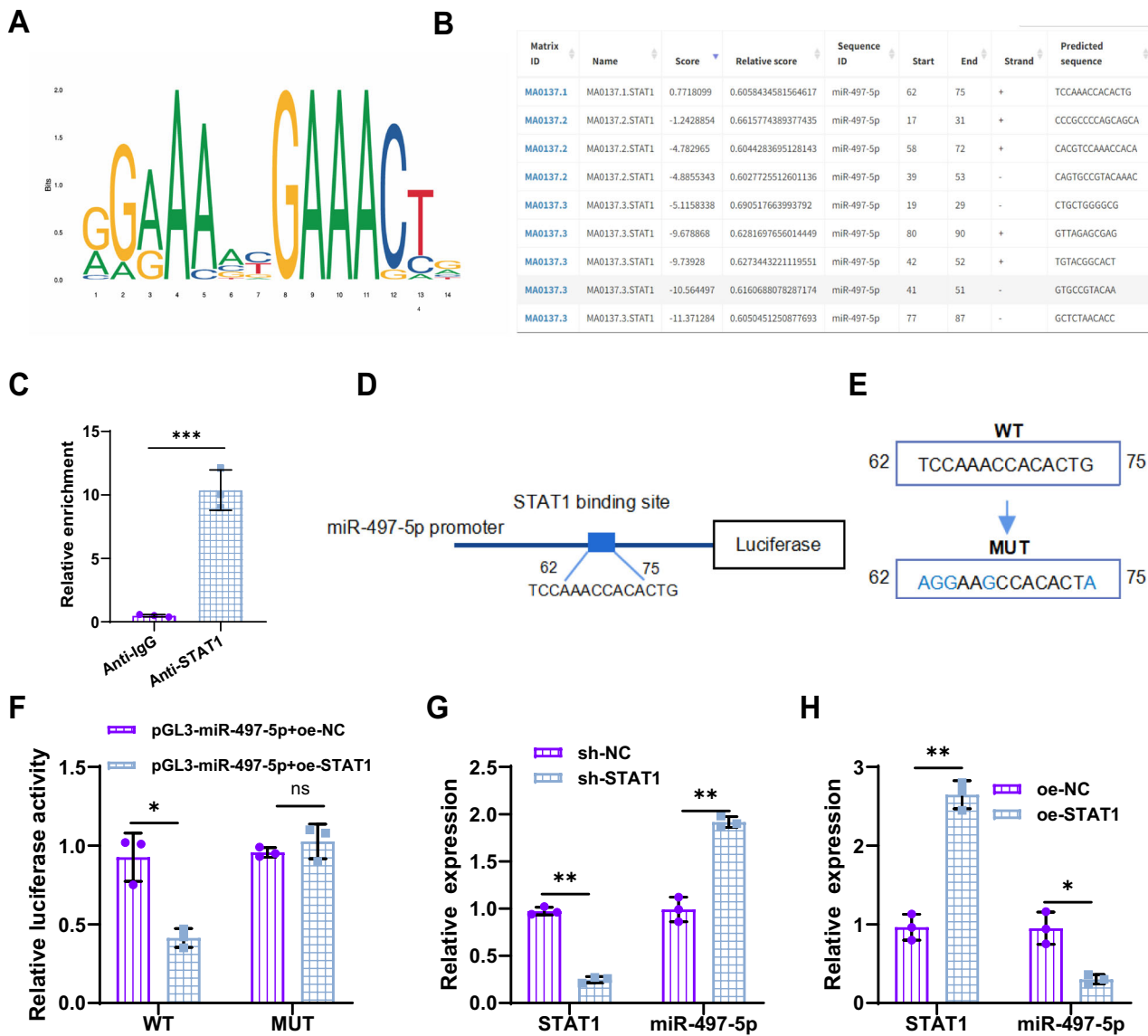


Fig. 4 | Transcriptional regulation of STAT1 on miR-497-5p. (A-B) JASPER database predicted the transcriptional sequence of STAT1 and its binding to the miR-497-5p promoter; (C) ChIP assay detected the enrichment of STAT1 in the miR-497-5p promoter region in HEK-293T cells; (D) Illustration of binding sites between STAT1 and the miR-497-5p promoter region; (E) Illustration of binding sites between wild-type and mutant sequences; (F) Dual-luciferase reporter gene

assay detected the transcriptional regulation activity of STAT1 on miR-497-5p in HEK-293T cells; (G-H) Expression levels of STAT1 and miR-497-5p were detected by RT-qPCR after silencing or overexpressing STAT1 in HEK-293T cells. Data are presented as mean \pm standard deviation. All cell experiments were repeated three times. Comparison between the two groups was analyzed using * $P < 0.05$, ** $P < 0.01$, *** $P < 0.001$, and ns denotes no significant difference.

compared to the oe-NC group (Fig. 4G, H). These findings suggest that *Stat1* can transcriptionally suppress the expression of *miR-497-5p*.

miR-497-5p exerts a protective effect against cell damage and apoptosis induced by *Stat1* overexpression

To explore the regulation of the *Stat1*/miR-497-5p axis in HIRI, we intervened in the expression of *Stat1* and *miR-497-5p* in an in vitro H/R cell

model. Cells were divided into three groups: oe-NC+Lv-NC group, oe-*Stat1* + Lv-NC group, and oe-*Stat1* + Lv-*miR-497-5p* group. The overexpression efficiency of *Stat1* and *miR-497-5p* was detected by RT-qPCR (Supplementary Fig. 8B). CCK-8 assay results demonstrated that overexpressing *miR-497-5p* effectively restored the cellular viability that was reduced due to *Stat1* overexpression (Fig. 5A, Supplementary Fig. 10A). Flow cytometry and TUNEL analysis revealed a significant increase in cell

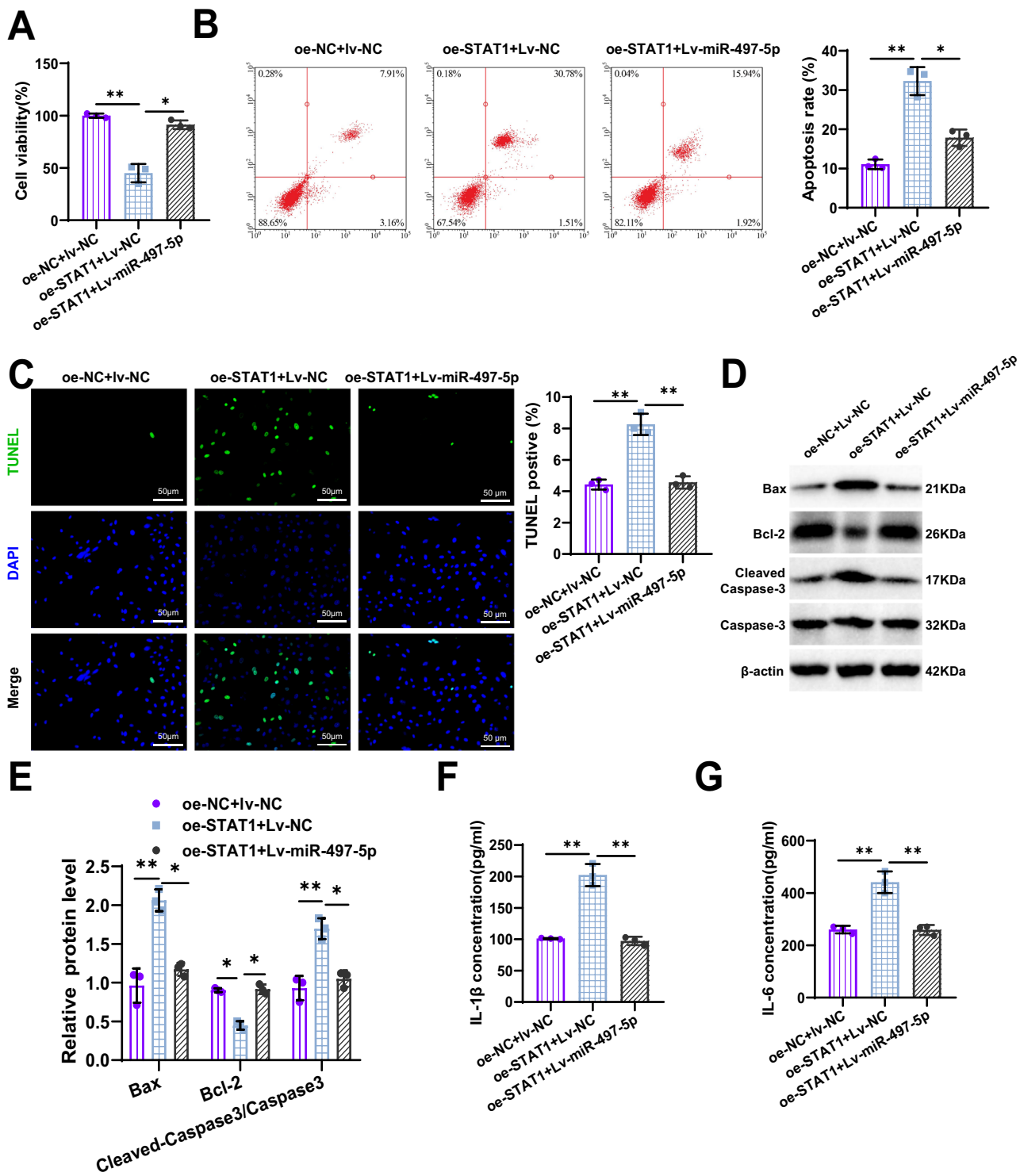


Fig. 5 | Effects of STAT1 on the regulation of miR-497-5p in the H/R model. (A) CCK-8 assay to measure the activity of H/R cells; (B) Flow cytometry to detect apoptosis rates of cells in each group, with corresponding statistical graph; (C) TUNEL fluorescence staining to observe apoptosis in cells from each group, with corresponding statistical graph (scale bar: 50 μm); (D, E) Western blot analysis to measure the protein expression levels of apoptosis markers Bax, Bcl-2, cleaved

Caspase-3, and Caspase-3 in cells from each group, with corresponding statistical graph; (F, G) ELISA to assess the expression of inflammatory factors IL-1 β and IL-6 in cells from each group. Values are presented as mean \pm standard deviation. All cell experiments were repeated three times. Statistical comparisons between groups were determined using $^*P < 0.05$, $^{**}P < 0.01$.

apoptosis in cells overexpressing *Stat1*. However, co-overexpression of *miR-497-5p* substantially alleviated cell apoptosis (Fig. 5B, C, Supplementary Fig. 10B), as evidenced by reduced expression of Bax and cleaved caspase-3 and increased expression of Bcl-2 (Fig. 5D, E, Supplementary Fig. 10C, D). Furthermore, *miR-497-5p* overexpression resulted in a decrease in the

expression of the inflammatory factors IL-1 β and IL-6 (Fig. 5F, G, Supplementary Fig. 10E, F).

In conclusion, the overexpression of *miR-497-5p* can mitigate H/R cell damage induced by *Stat1* overexpression, reduce cell apoptosis, and affect the expression of related inflammatory factors.

miR-497-5p regulates cell death and inflammation in HIRI by targeting HDAC7

To gain a comprehensive understanding of the crucial role of *miR-497-5p* in regulating cell death and inflammation mediated by *Stat1* in HIRI, we investigated the expression profile of *miR-497-5p* in the human miRNA tissue atlas using miRTarBase (Supplementary Fig. 9F). Additionally, we performed an enrichment analysis of the has-*miR-497-5p* targets in KEGG pathways using StarBase (Supplementary Fig. 9G).

To further explore the molecular mechanism of *miR-497-5p* in HIRI, we utilized miRNA target gene prediction websites to identify downstream targets of *miR-497-5p*. Through StarBase, miRmap, miRWalk, and mirDIP, we predicted a total of 2831, 3121, 6199, and 7079 potential target genes, respectively. Afterward, we intersected these predicted targets with the DEGs obtained from the transcriptome sequencing dataset, resulting in 9 candidate target genes (Fig. 6A). Subsequently, we conducted GO/KEGG enrichment analysis on these candidate genes, revealing their involvement in specific pathways such as Histone H3 deacetylation, I-kappaB phosphorylation, and negative regulation of NIK/NF-kappaB signaling pathway (Fig. 6B). Notably, HDAC7 plays a vital role in gene expression regulation, cell cycle, and cell death processes, and it may contribute significantly to HIRI through protein modifications^{33,34}. Consistently, bioinformatics predictions from multiple websites indicated HDAC7 as a target of *miR-497-5p* (Fig. 6C). We observed no significant changes in HDAC7 expression levels in the proteome dataset, whereas in the transcriptome dataset, the expression of HDAC7 in the HIRI group was significantly upregulated compared to the normal group (Fig. 6D). Subsequently, using RT-qPCR, we measured the expression of HDAC7 in the HIRI mouse model and H/R cell model, demonstrating a significant increase in HDAC7 expression in the model group compared to the normal control group (Fig. 6E, F). In addition, there was a significant negative correlation between the expression of *miR-497-5p* and HDAC7 (Fig. 6G).

We validated the targeting binding of *miR-497-5p* and HDAC7 through a dual-luciferase reporter gene assay in HEK-293T cells. The results showed that overexpression of *miR-497-5p* suppressed the relative luciferase activity of wild-type HDAC7 3'-UTR, whereas no significant change was observed in the mutant-type HDAC7 group (Fig. 6H, I). Furthermore, we manipulated the expression of *miR-497-5p* and measured the changes in HDAC7 expression in cells. The results revealed a significant upregulation of HDAC7 expression upon the inhibition of *miR-497-5p*, while overexpression of *miR-497-5p* led to a significant downregulation of HDAC7 expression (Fig. 6J, K).

In conclusion, *miR-497-5p* can target and inhibit the expression of HDAC7.

Stat1 regulates the *miR-497-5p*/HDAC7 pathway to promote the progression of hepatocellular ferroptosis in HIRI

Ferroptosis, as a distinct form of non-apoptotic cell death, has garnered extensive attention in recent years for its role and regulation in liver ischemia-reperfusion injury (IRI). Numerous studies have demonstrated the involvement of ferroptosis in the onset and progression of HIRI^{3,35,36}. The high-throughput transcriptomic and proteomic investigations mentioned above revealed DEGs and proteins that are associated with ferroptosis (Fig. 7A). We postulate that *Stat1* regulates the *miR-497-5p*/HDAC7 pathway to promote hepatocellular ferroptosis in HIRI.

To validate this finding, we employed the fluorescent probe 2',7'-dichlorofluorescein diacetate (DCFH-DA) to measure total intracellular reactive oxygen species (ROS) levels and mitochondrial ROS content. Experimental results indicated that H/R treatment significantly increased cellular ROS levels, whereas downregulation of *Stat1* significantly reduced ROS levels. Conversely, under conditions of *miR-497-5p* knockdown, ROS levels were markedly elevated once again (Fig. 7B, Supplementary Fig. 11A).

Furthermore, we assessed specific markers of ferroptosis, including malondialdehyde (MDA), superoxide dismutase (SOD), and reduced glutathione (GSH). The results demonstrated a significant increase in MDA but a substantial decrease in GSH and SOD in cells subjected to H/R treatment.

Knockdown of *Stat1* attenuated the progression of ferroptosis, while knockdown of *miR-497-5p* exacerbated ferroptosis (Fig. 7C–E, Supplementary Fig. 11B–D). To quantitatively analyze intracellular Fe²⁺ levels, we utilized the orange iron staining method combined with Prussian blue staining to observe color changes resulting from Fe²⁺ accumulation. Experimental outcomes revealed that both H/R treatment and *miR-497-5p* knockdown led to an increase in intracellular Fe²⁺ accumulation, indicative of activation of the ferroptosis pathway, whereas downregulation of *Stat1* facilitated the restoration of iron metabolism balance and alleviated the process of ferroptosis (Fig. 7F, G, Supplementary Fig. 11E, F).

Overall, *Stat1* promotes ROS generation and ferroptosis in HIRI through the regulation of *miR-497-5p*. This process significantly exacerbates the cellular damage and Fe²⁺ accumulation induced by H/R treatment.

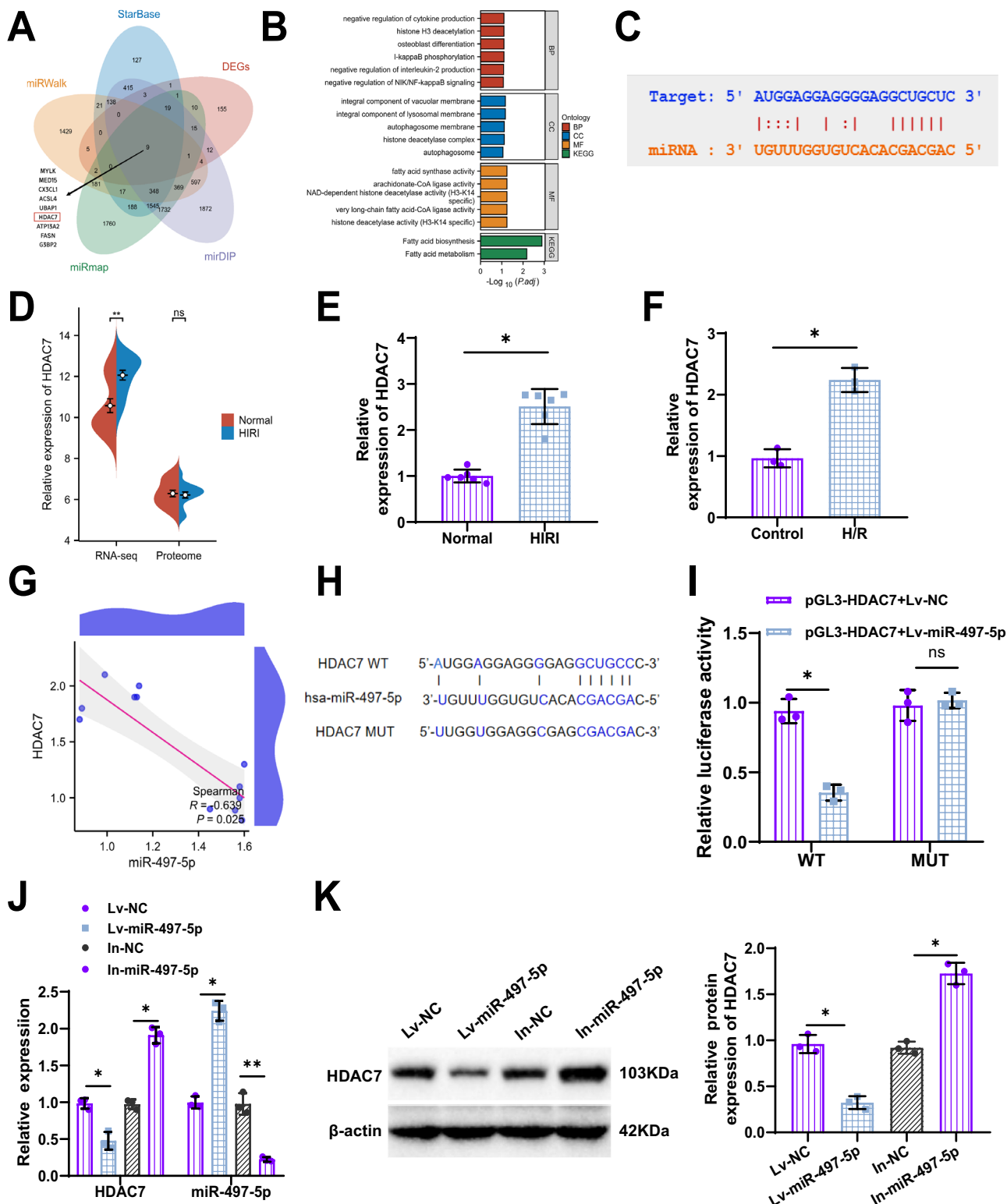
To investigate whether *Stat1* regulates the impact of HDAC7 on ferroptosis and inflammatory response in HIRI, we conducted an in vitro experiment using an H/R cell model and intervened in the expression of *Stat1* and HDAC7. The cells were divided into the oe-NC+sh-NC group, oe-*Stat1*+sh-NC group, and oe-*Stat1*+sh-HDAC7 group. We assessed the overexpression efficiency of *Stat1* and the silencing efficiency of HDAC7 using RT-qPCR (Supplementary Fig. 8C). The CCK-8 experimental results showed that silencing of HDAC7 effectively restored cellular viability and improved the decrease caused by overexpression of *Stat1* (Supplementary Fig. 12A). Furthermore, the silencing of HDAC7 significantly reduced the expression levels of the inflammatory factors IL-1 β and IL-6 (Supplementary Fig. 12B, C). Silencing of HDAC7 also mitigated the oxidative stress induced by overexpression of *Stat1* (Supplementary Fig. 12D). Changes in the specific indicators of ferroptosis, MDA, SOD, and GSH, demonstrated that silencing of HDAC7 effectively decreased ferroptosis (Supplementary Fig. 12E–G). Additionally, silencing of HDAC7 helped restore the iron metabolism imbalance caused by overexpression of *Stat1* (Supplementary Fig. 12H, I). In addition, consistent trends were observed in AML12 cells, further confirming the regulatory effects of Rb1 (Supplementary Fig. 13).

In summary, *Stat1* promotes the production of ROS and ferroptosis by inhibiting *miR-497-5p*, thereby exacerbating cell damage and accumulation of Fe²⁺. Both upregulation of *miR-497-5p* and silencing of HDAC7 effectively alleviate these effects caused by *Stat1*, reducing ferroptosis and inflammatory response, thus protecting cells from HIRI-induced damage.

In vivo validation of *Stat1* transcriptional repression of *miR-497-5p* to activate HDAC7 promoting hepatic iron-mediated cell death and inflammatory response

In our in vitro experiments, we confirmed that *Stat1* can transcriptionally suppress the expression of *miR-497-5p*, thereby promoting hepatic iron-mediated cell death (H/R) and inflammatory response through HDAC7 targeting. To validate this mechanism in vivo, we first constructed murine HDAC7 overexpression plasmids and *Stat1* knockdown sequences and verified the efficacy of the *Stat1* knockdown sequence. In subsequent experiments, we selected sh-*Stat1*#2 (hereinafter referred to as sh-*Stat1*) due to its higher knockdown efficiency (Supplementary Fig. 8D). The expression levels of *Stat1* knockdown and HDAC7 overexpression in mouse liver tissue were detected by RT-qPCR (Supplementary Fig. 8E). Then, in the HIRI mouse model, HDAC7 overexpression and *Stat1* knockdown were mediated by intravenous injection of lentiviral vectors.

Liver H&E staining revealed that *Stat1* knockdown significantly alleviated liver damage, while under conditions of HDAC7 overexpression, the severity of liver damage increased again (Fig. 8A, B). Furthermore, similar results were obtained by collecting peripheral blood from the mice and measuring ALT, AST, as well as the levels of the inflammatory factors IL-1 β and IL-6 (Fig. 8C–F). Moreover, the levels of MDA, SOD, and GSH in mouse liver samples were determined. The results showed that the concentration of MDA decreased significantly after *Stat1* knockdown, while the levels of SOD and GSH increased significantly; however, HDAC7 overexpression reversed these effects (Fig. 8G–I). Prussian blue staining was also used to measure the iron ion content in liver tissues, and the results similarly



HIRI mice (Normal = 6, HIRI = 6); (H) Binding sites between *miR-497-5p* and the wild-type and mutant 3'UTR of HDAC7; (I) Dual-luciferase reporter gene experiment confirming the targeted binding relationship between *miR-497-5p* and HDAC7; (J) RT-qPCR analysis of *miR-497-5p* and HDAC7 expression in cells after overexpression or inhibition of *miR-497-5p*; (K) Western blot analysis of HDAC7 expression in HEK-293T cells after silencing or overexpression of *miR-497-5p*. Values are presented as mean \pm standard deviation. All cell experiments were repeated three times. Statistical comparisons between groups were determined using **P* < 0.05, ***P* < 0.01, and ns denotes no significant difference.

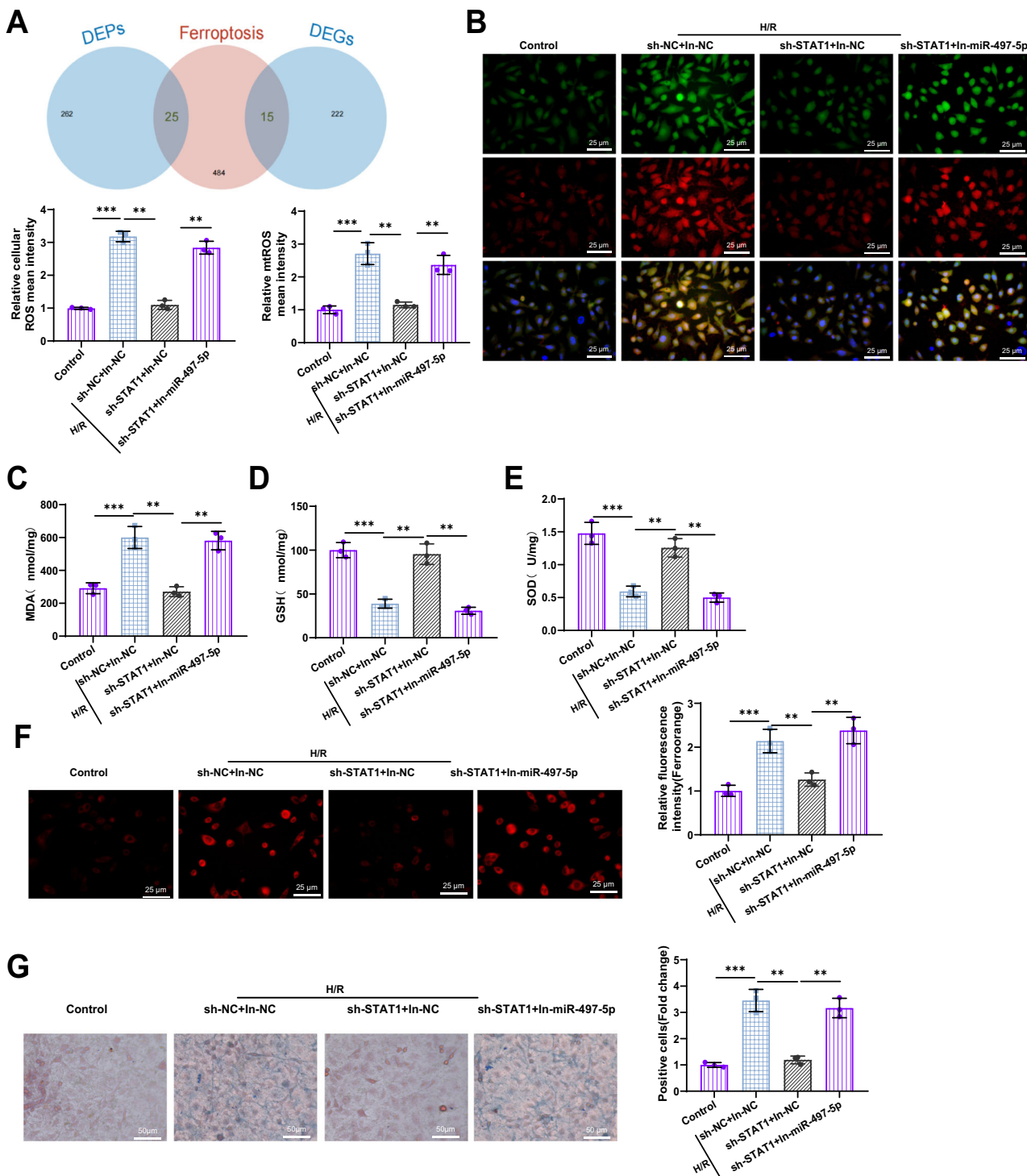


Fig. 7 | Investigation of STAT1's regulation of miR-497-5p in iron-induced cell death during H/R. (A) Venn diagram showing the intersection between DEGs/proteins related to iron-induced cell death in transcriptome sequencing and proteomics; (B) Quantification and visualization of cellular ROS (green) and mtROS (red) levels in liver cells, with corresponding statistical graph (scale bar: 25 μm); (C–E) Changes in the levels of iron-death-specific indicators MDA, GSH, and SOD in

liver cells; (F) Representative confocal microscopy images of liver cells stained with orange iron dye, with corresponding statistical graph (scale bar: 25 μm); (G) Visualization and statistical graph of Fe²⁺ content in cells using Prussian blue staining (scale bar: 50 μm). All cell experiments were repeated three times. Values are presented as mean ± standard deviation. Statistical comparisons between groups were determined ***P* < 0.01, ****P* < 0.001, and ns denotes no significant difference.

showed that *Stat1* knockdown significantly reduced the iron ion content, while HDAC7 overexpression significantly increased it (Fig. 8j).

In summary, we discovered that *Stat1* activates HDAC7 by transcriptionally repressing *miR-497-5p*, thereby promoting iron-mediated cell death and inflammatory response in HIRI. In our *in vivo* experiments, we

validated this mechanism, indicating that *Stat1* knockdown could alleviate liver injury and inflammatory response caused by HIRI, as well as reduce iron ion content. On the other hand, HDAC7 overexpression reversed these effects, highlighting the important role of *Stat1*, *miR-497-5p*, and HDAC7 in regulating HIRI.

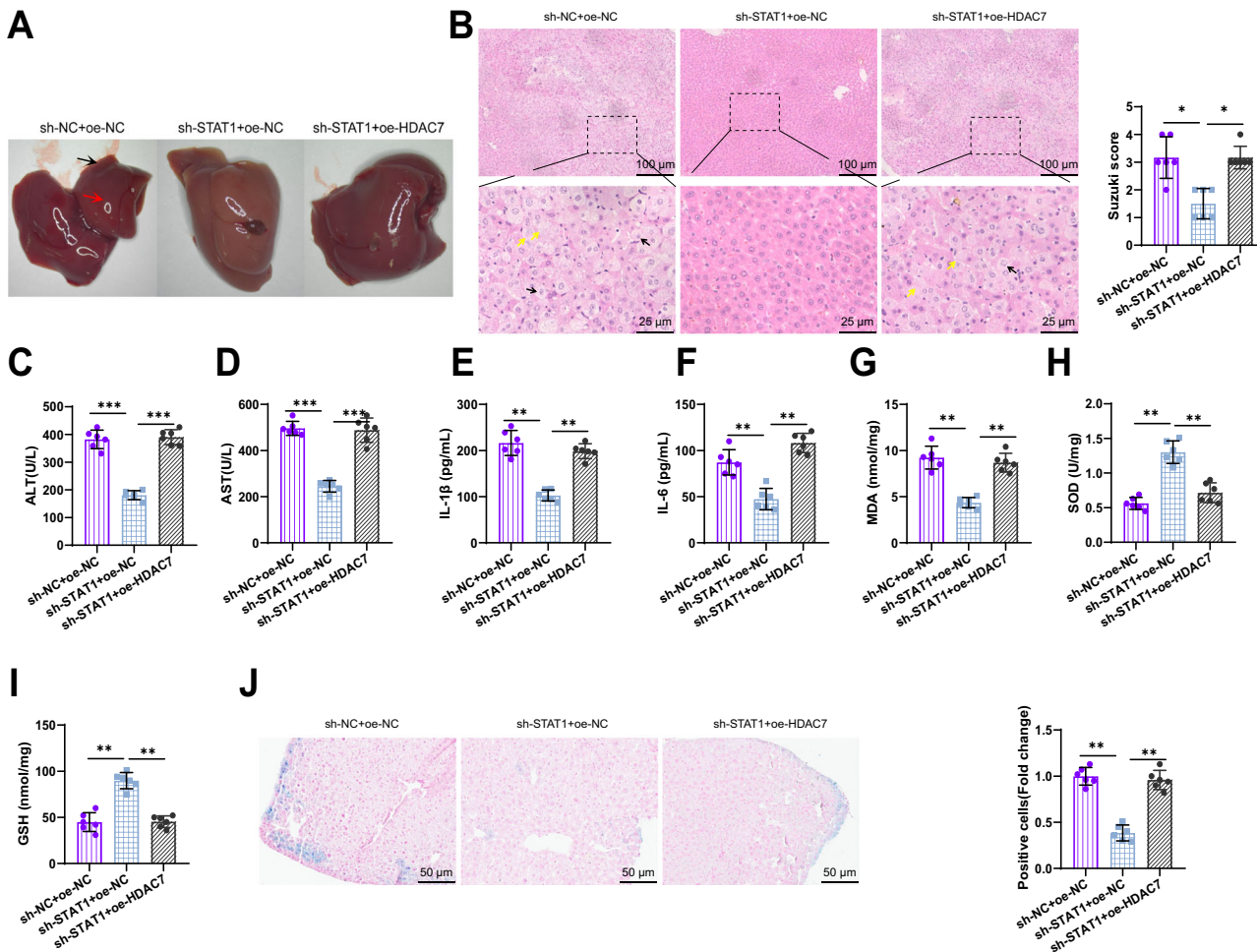


Fig. 8 | Validation of the effects of STAT1-mediated *miR-497-5p*/HDAC7 on HIRI Ferroptosis and inflammatory response in vivo. (A) Gross morphology of the liver in each group, black arrows indicate hepatic congestion, and red arrows denote lobular swelling; (B) Representative H&E stained images of the liver (scale bar: 100 μ m/25 μ m) and evaluation of liver tissue damage according to Suzuki's histological criteria. Yellow arrows indicate vacuole formation, and black arrows indicate hepatocellular necrosis; (C–F) Levels of ALT, AST, IL-1 β , and IL-6 in

peripheral blood of mice; (G–I) Changes in the content of ferroptosis-specific markers MDA, GSH, and SOD in liver cells; (J) Detection of Fe²⁺ content in cells using Prussian blue staining (scale bar: 50 μ m), with statistical graph provided. Each group of mice contained 6 individuals, and the values represent the mean \pm standard deviation. Comparisons between groups were denoted by asterisks: * P < 0.05, ** P < 0.01, *** P < 0.001.

Discussion

HIRI is a complex pathological process that is frequently observed during liver surgery^{7,16,37}. This study aims to investigate the underlying mechanisms of *Stat1* in HIRI and its regulation of ferroptosis and inflammatory response through the modulation of the non-coding *miR-497-5p* and its downstream target genes. HIRI, caused by ischemia and reperfusion, can lead to severe liver dysfunction, cellular apoptosis, and inflammatory response³⁸. To gain a better understanding of the pathogenesis of HIRI and identify potential therapeutic targets, comprehensive investigations were conducted using a mouse model and *in vitro* cellular models of HIRI.

The study revealed that *Stat1*, highly expressed in HIRI, is involved in multiple signaling pathways associated with ferroptosis and inflammatory response. These findings are consistent with previous research, indicating the crucial regulatory role of *Stat1* in HIRI¹⁴. Previous studies have also identified the regulatory relationship between *Stat1* and inflammation-related genes and cytokines^{39–41}. Thus, this study provides further support for the key role of *Stat1* in HIRI and offers new clues for further exploration of its regulatory mechanisms.

Furthermore, the study found significant enrichment of *Stat1* in the *miR-497-5p* promoter region, which can transcriptionally suppress the expression of *miR-497-5p*. These findings are in line with previous research, suggesting the possible regulation of *miR-497-5p* by *Stat1* in

HIRI¹⁹. In other diseases, *miR-497-5p* has been demonstrated to have inhibitory effects on inflammation and cellular apoptosis. Hence, this study further supports the regulatory role of *miR-497-5p* in HIRI and demonstrates the potential mechanism by which *Stat1* regulates this pathway¹⁹. Moreover, numerous proteins have been previously implicated in the development and progression of HIRI^{42,43}. Although the role of microRNAs (miRNAs) in HIRI remains a subject of ongoing investigation, growing evidence indicates that miRNAs play critical roles in this pathological process. For example, Huang et al. demonstrated that suppression of *miR-450b-5p* mitigated HIRI by targeting *CRYAB*⁴⁴. In another study, Huang et al. showed that *miR-125b* protects the liver from HIRI by inhibiting *RAF6* and *NF- κ B* pathways⁴⁵. While proteins exert their regulatory roles through diverse targets, the influence of miRNAs on HIRI via mechanisms such as autophagy, apoptosis, oxidative stress, and inflammation cannot be overlooked¹⁶.

In addition, the study discovered that the activation of HDAC7 by *Stat1* could potentially influence HIRI. HDAC7 is a histone deacetylase with unclear mechanisms of action in HIRI^{46–48}. Previous studies associated with HIRI have implicated HDAC7 in signaling pathways related to cellular apoptosis, inflammation, and oxidative stress¹⁴. Therefore, these findings provide possibilities for further research on the mechanisms of HDAC7 in HIRI and its potential therapeutic targets.

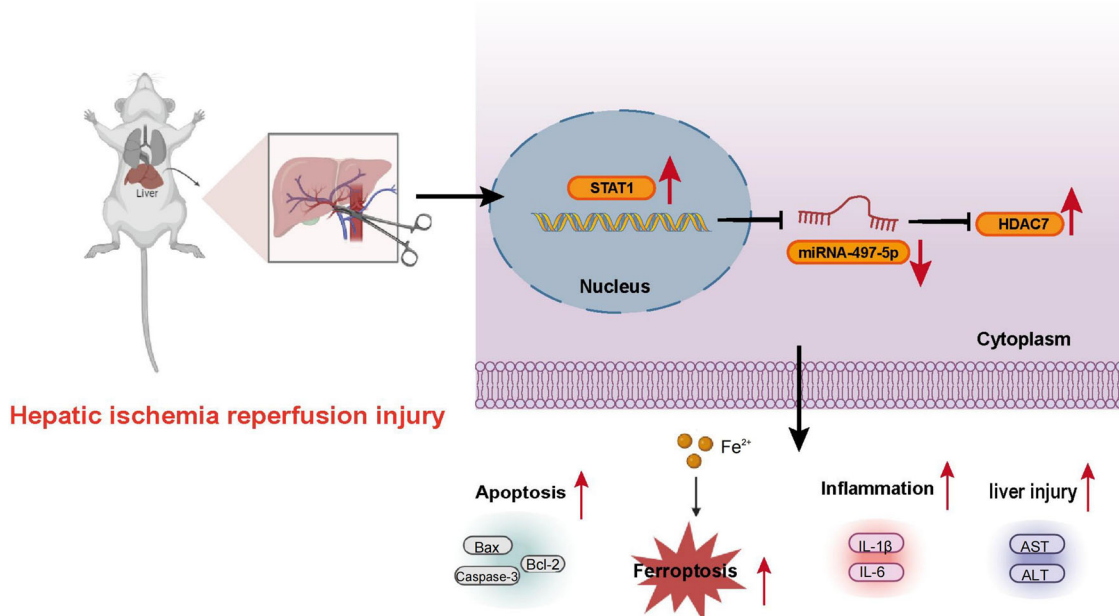


Fig. 9 | Schematic diagram of the molecular mechanism of STAT1 involvement in HIRI ferroptosis and inflammatory response based on multi-omics and in vitro and in vivo experiments. (Created by BioRender).

The current study shares similarities with previous research findings but also presents some differences. Previous studies have already identified the association of *Stat1* with HIRI and revealed its involvement in cellular apoptosis and inflammatory response¹⁴. However, this study further elucidates the details of *Stat1*'s regulation of the *miR-497-5p* and HDAC7 pathways, providing a deeper understanding of the pathogenesis of HIRI¹⁹. Additionally, this study offers new insights into the regulation of HDAC7, expanding the research scope of HIRI. Consistent with our previous results, we verified the functional mechanism of *Stat1* in both human hepatocytes (MIHA) and mouse hepatocytes (AML12) during HIRI. However, numerous studies have emphasized that in addition to hepatocytes, liver non-parenchymal cells also play indispensable roles in HIRI. For instance, Li et al. demonstrated that the immune responses of Kupffer cells critically affect HIRI outcomes⁴⁹. Huang et al. showed that the miR-22/FAM49B axis regulates Kupffer cell immune activation via the Rac1/TRA6/IKK pathway⁵⁰. Similarly, Hu et al. reported that HSP110 aggravates HIRI by promoting the immune response of Kupffer cells through activation of the NF- κ B pathway⁵¹. Therefore, it remains essential to verify whether the mechanisms we identified are specific to hepatocytes or extend to other hepatic cell populations.

In summary, *Stat1* plays a central regulatory role in the key pathological mechanisms and regulates the occurrence and progression of ferroptosis and inflammatory response in HIRI by suppressing the transcription of *miR-497-5p* and activating HDAC7. Through the comprehensive use of transcriptomics and proteomics, we not only explored the complex mechanisms of HIRI in depth but also revealed for the first time the interaction and importance of *Stat1*, *miR-497-5p*, and HDAC7 in ferroptosis and inflammatory response. This significant finding not only provides a new perspective for understanding the molecular mechanisms of liver ischemia-reperfusion injury but also indicates potential therapeutic targets and offers new hope for HIRI treatment (Fig. 9).

The scientific value of this study lies in the in-depth exploration of the role of *Stat1* in HIRI and the regulation of ferroptosis and inflammatory response through the mediation of non-coding small RNA (*miR-497-5p*) and downstream target genes. Through a combination of transcriptomics, proteomics, and other omics approaches, we revealed the key regulatory pathways and crucial genes/proteins involved in HIRI. Additionally, through studies using a H/R cell model and in vivo mouse experiments, we

further established the important role of *Stat1* in regulating *miR-497-5p* and HDAC7 and identified its association with HIRI.

The clinical significance of this study lies in providing new research directions for understanding the molecular mechanisms underlying the occurrence and progression of HIRI. By elucidating the role of *Stat1* in HIRI and its regulatory relationship with *miR-497-5p* and HDAC7, this study offers possibilities for developing new treatment strategies and drug targets. Targeted regulation of molecules such as *Stat1*, *miR-497-5p*, and HDAC7 may effectively alleviate the severity of liver function damage, inflammatory response, and ferroptosis caused by HIRI, which is of great significance for the postoperative recovery and quality of life of liver surgery patients.

However, this study also has some limitations. Firstly, although we conducted in-depth studies using mouse models and cell experiments, the results may not fully reflect the actual situation of human HIRI due to limitations in experimental conditions and animal models. Moreover, all experiments in this study were conducted using male mice to avoid hormonal variability. While this approach improves consistency, it limits the generalizability of our findings. Given potential sex-based differences in immune responses and susceptibility to ferroptosis, future studies using female or mixed-sex cohorts are necessary to validate and expand upon our conclusions. Secondly, we only focused on the role of key factors such as *Stat1*, *miR-497-5p*, and HDAC7, while HIRI is a complex disease process that may involve other unexplored molecular mechanisms. Lastly, this study was conducted under laboratory conditions and further clinical research is needed to verify the feasibility and effectiveness of these findings.

In terms of future prospects, this study can be further expanded in terms of depth and breadth. In terms of depth, the regulatory mechanisms and interaction networks of *Stat1*, *miR-497-5p*, and HDAC7 can be further studied to explore more regulatory pathways and targets related to HIRI. In terms of breadth, more clinical studies can be conducted to validate the reliability and application value of these findings in human HIRI. In addition, by integrating the concept and technology of personalized medicine, treatment strategies based on key molecules such as *Stat1*, *miR-497-5p*, and HDAC7 can be combined with clinical practice to lay the foundation for personalized HIRI treatment. In conclusion, this study provides new ideas and directions for further in-depth research on the occurrence mechanisms of HIRI and related treatments, and it has significant scientific and clinical value.

Materials and methods

Construction and grouping of mouse models

The experimental protocol and animal usage plan have been approved by The First Affiliated Hospital of Xinjiang Medical University's Animal Ethics Committee (Approval No: A230307-81) and the Institutional Animal Care and Use Committee of the Affiliated Huai'an No.1 People's Hospital of Nanjing Medical University. Six-week-old male BALB/c mice (No. 211, Beijing Vitron Lihua Experimental Animal Technology Co., Ltd, Beijing, China) with a weight range of 17–21 g were used. The mice were housed under standard environmental conditions with a temperature of $23 \pm 2^\circ\text{C}$, humidity of $55 \pm 5\%$, and a 12 h light-dark cycle. The experiments were initiated after 1 week of acclimation to the environment. We have complied with all relevant ethical regulations for animal use.

Prior to the procedure, the mice were fasted for 12 h with no access to water for 4 h. The mice were anesthetized using 1.5% isoflurane (R510-22-10, Revo, Shenzhen, China), intubated through the oral cavity, and then connected to a rodent ventilator. After anesthetization, the mice were fixed in a supine position and subjected to a midline incision of the abdominal cavity. In the HIRI group, the left and middle lobes of the liver were separated, and blood flow was occluded using vascular clamps to achieve ~70% liver ischemia. Successful ischemia was indicated by a change in the color of the ischemic lobes from red to white. After 1 h of clamping, the clamps were released to restore the hepatic artery and portal vein blood supply to the ischemic lobes. Successful reperfusion was indicated by a change in the color of the ischemic lobes back to red. The reperfusion time in our HIRI model was 6 h following 1 h of ischemia⁴⁹. The normal control group underwent only a 30 min laparotomy without vascular occlusion. After completion of the surgery, the incision was closed layer by layer, and vital signs were monitored and recorded. The mice were euthanized by cervical dislocation at 6 h post-reperfusion (after restoration of blood flow). Liver and serum samples were collected for analysis^{52,53}.

The experiment was divided into the following groups: Normal control group (Normal group), Hepatic Ischemia-Reperfusion Injury group (HIRI group), sh-NC+oe-NC group (intravenous injection of sh-NC and oe-NC through the tail vein), sh-*Stat1*+oe-NC group (intravenous injection of sh-*Stat1* and oe-NC through the tail vein), and sh-*Stat1*+oe-HDAC7 group (intravenous injection of sh-*Stat1* and oe-HDAC7 through the tail vein). The slow virus was injected through the tail vein, with a working titer of 5×10^6 TU/mL and an injection volume of 10 μL per mouse, followed by continuous injections for 1 week⁵⁴.

RNA extraction and sequencing

Total RNA was extracted from the livers of both model and control mice, with 15 samples taken from each group. Trizol reagent (15596026, Invitrogen, Car, Cal, USA) was utilized for total RNA isolation. The concentration and purity of RNA samples were determined using the Agilent 2100 Bioanalyzer (G2939B, Agilent, USA). Total RNA samples meeting the following criteria were used for subsequent experiments: RNA Integrity Number (RIN) ≥ 7.0 and 28S:18S ratio ≥ 1.5 .

Sequencing libraries were generated and sequenced by CapitalBio Technology (Beijing, China). A total of 5 μg of RNA was used per sample. Briefly, Ribo-Zero™ Magnetic Kit (MRZE706, Epicentre Technologies, Madison, Wisconsin, USA) was employed for the removal of ribosomal RNA (rRNA) from total RNA. NEB Next Ultra RNA Library Prep Kit (#E7775, NEB, USA) was used for Illumina library construction and sequencing. Subsequently, RNA fragments were fragmented into ~300 base pair (bp) fragments in NEB Next First Strand Synthesis Reaction Buffer (5 \times). The first-strand cDNA was synthesized using reverse transcriptase primers and random primers, while the second-strand cDNA was synthesized in the second-strand synthesis reaction buffer containing dUTP Mix (10 \times). The cDNA fragments underwent end repair, including the addition of polyA tails and the connection of sequencing adapters. After linking Illumina sequencing adapters, the second strand of cDNA was digested using USER Enzyme (#M5508, NEB, USA) to construct strand-specific libraries. The library DNA was amplified, purified, and enriched by PCR.

Finally, the library was assessed on the Agilent 2100 and quantified using the KAPA Library Quantification Kit (KK4844, KAPA Biosystems). Paired-end sequencing was performed on the NextSeq CN500 (Illumina) sequencer with an average sequencing depth of $50 \times$ ^{55,56}.

Quality control and differential expression analysis

The quality of paired-end reads from raw sequencing data was assessed using FastQC software v0.11.8. Preprocessing of the raw data was performed using Cutadapt software 1.18, which involved the removal of Illumina sequencing adapters and poly(A) tail sequences. Reads with an N content exceeding 5% were filtered out using a Perl script. The FASTX Toolkit software 0.0.13 was used to extract 70% of reads with base quality scores above 20. The BBMap software was employed to repair the paired-end sequences. Finally, the filtered and high-quality read fragments were aligned to the Rnor_6.0 reference genome provided by Gencode using hisat2 software 0.7.12. Differential gene expression analysis (DEGs) between normal and HIRI model samples was performed using the Limma package in R software, with thresholds set at $|\log_2\text{FC}| > 1$ and $P\text{-value} < 0.05$. PCA was carried out using the prcomp function in the stats package of R. The differential gene expression heat map was generated using the heatmap package, and the volcano plot for differential gene expression was created using the ggplot2 package. GO and KEGG enrichment analysis was performed using the clusterProfiler package, while gene set enrichment analysis was conducted using the gene set variation analysis (GSVA) package. WGCNA was performed using the WGCNA package^{57,58}.

Construction of WGCNA

In this section, we used the R software and the following packages: matrixStats, Hmisc, foreach, doParallel, fastcluster, dynamicTreeCut, survival, and WGCNA. Firstly, we removed the normal dataset, checked for missing values, and eliminated outlier samples. Next, we clustered the samples based on gene expression levels. Then, we constructed a scale-free network using the power value selected from the Pearson correlation coefficient between genes, considering the average connectivity of the correlation coefficient R^2 in both the scale-free network fitting process and the scale-free network model. We chose a power value of 20. We constructed a distance matrix among genes based on the power value and then performed clustering. We calculated the within-module connectivity of genes with similar expression profiles using the topological overlap measure (TOM). Finally, we used a dynamic hybrid cut method to partition these genes into different modules and selected the module with the highest mRNA correlation. Subsequently, we used the “VennDiagram” package to conduct Venn analysis and filtered the intersection of this module's genes and the DEGs in the transcriptome as the key genes^{59,60}.

Sample preparation and determination of the proteomic profile

Fifteen liver tissue samples were collected from both the control group and the experimental group of mice. The samples were individually ground into powder using liquid nitrogen and transferred to 5 cm^3 centrifuge tubes. Subsequently, an ultrasonic cell disrupter (SCIENTZ-IIID, Scientz, Ningbo, China) was employed for sonication in an ice bath. The sonication was performed using a phenol-based extraction buffer that consisted of 10 mM DTT (R0861, MBI, Beijing, China), a 1% mixture of protease inhibitors (P6731, Solarbio, Beijing, China), and 2 mM EDTA (E1170, Solarbio, Beijing, China). This step was repeated eight times. Following this, an equal volume of pH 8.0 Tris-saturated phenol (HC1380, Vaner, Beijing, China) was added, and the mixture was vortexed for 4 min. Next, the mixture was centrifuged at 4°C at a force of $5000 \times g$ for 10 min, and the upper phenol layer was transferred to a new centrifuge tube. To the phenol solution, a 0.1 M ammonium sulfate (101217, Merck, USA) saturated methanol (106035, Merck, USA) solution was added at a volume ratio of 1:5, and the mixture was left overnight to precipitate the proteins. Subsequently, the supernatant was removed after centrifugation at 4°C for 10 min. Finally, the remaining precipitate was washed once with cold methanol and three times with cold acetone. The washed protein was then dissolved in 8 M urea

(U8020, Solarbio, Beijing, China), and the protein concentration was determined using the BCA assay kit (P0012, BioTek, Shanghai, China) according to the manufacturer's instructions⁶¹.

Enzymatic digestion and mass spectrometry analysis

Each sample was subjected to enzymatic digestion using 50 µg of protein. The protein solution was mixed with DTT to achieve a concentration of 5 mM and incubated at 56 °C for 30 min. Acetamide (822343, Merck, USA) was added to the solution to a final concentration of 11 mM and incubated in a dark room at room temperature for 15 min. Subsequently, the sample was diluted to a urea concentration below 2 M, and trypsin (25200056, Thermo Fisher Scientific, USA) was added at a ratio of 1:50 (w/w) enzyme to protein, followed by overnight digestion at 37 °C. Afterward, trypsin was added at a ratio of 1:100 (enzyme to protein), and digestion was continued for an additional 4 h.

Following trypsin digestion, the peptide fragments were desalting using HyperSep™ C18 purification columns (60108-302, Thermo Fisher Scientific, USA), followed by vacuum drying. The peptides were then dissolved in 0.5 M triethylammonium bicarbonate (TEAB) (90114, Thermo Fisher Scientific, USA) and processed according to the manufacturer's instructions of the Tandem Mass Tag (TMT) reagent kit (90064CH, Thermo Fisher Scientific, USA). In brief, one unit of TMT reagent was thawed and reconstituted in acetonitrile (113212, Merck, USA). The peptide mixture was then incubated at room temperature for 2 h, followed by vacuum centrifugation, desalting, and drying. Equal amounts of labeled peptide fractions were combined and subjected to fractionation using the Pierce™ High pH Reversed-Phase Peptide Separation Kit (84868, Thermo Fisher Scientific, USA). Finally, the samples were collected and pooled into 15 fractions, and the dried peptides were resuspended in 0.1% formic acid (159002, Merck, USA).

For separation, 2 µg of peptide fragments from each sample were loaded onto an Easy nLC 1200 nano-UPLC system (Thermo Fisher Scientific, USA). The samples were injected into a Trap C18 chromatographic column (100 µm × 20 mm, 5 µm) and subsequently separated using a C18 analytical column (75 µm × 150 mm, 3 µm) with a flow rate of 300 nL/min. The mobile phases used were: (A) 0.1% formic acid aqueous solution and (B) 0.1% formic acid in water-acetonitrile (containing 95% acetonitrile). The gradient elution program was as follows: 0 → 2 min, 2% → 8% B; 2 → 71 min, 8% → 28% B; 71 → 79 min, 28% → 40% B; 79 → 81 min, 40% → 100% B; 81 → 90 min, 100% B. The separated peptides were then subjected to mass spectrometry analysis using a Q-Exactive HF-X mass spectrometer (Thermo Fisher Scientific, USA). The analysis duration was 60 min with an electrospray voltage of 2.1 kV. The detection mode was positive ionization, and the precursor ion scan range was set from 350 to 1200 m/z. The first-level mass resolution was set at 60000 @ m/z 200, with an automatic gain control (AGC) target of 3e6 and a maximum injection time of 30 ms. The second-level mass resolution was set at 15000 @ m/z 200, with an AGC target of 1e6 and a maximum injection time of 25 ms. The MS2 activation type was high-energy collision-induced dissociation (HCD), with an isolation window of 20 Th and a normalized collision energy of 32^{61,62}.

Database retrieval and data processing

The LC-MS/MS data obtained was processed using MaxQuant software (v.1.5.2.8) for peptide identification and protein quantification. The UniProt 14.1 (2009) - *Gossypium hirsutum* database, along with the reverse bait database, was employed for tandem mass spectrometry retrieval. Trypsin/P was designated as the cleaving enzyme, allowing for up to 2 missed cleavages. The initial search was conducted with a 20 ppm tolerance, followed by a main search using a 5 ppm tolerance for fragment ion masses. Peptide false discovery rate (FDR) ≤ 0.01, protein FDR ≤ 0.01, and peptide score distribution were employed as filtering criteria. Differential expression proteins (DEPs) were screened using the "Limma" package in R software, with a threshold of $|\log_2\text{FC}| > 1$ and $P\text{-value} < 0.05$ to identify DEPs between the normal and HIRI samples. PCA was performed using the "prcomp" function in the "stats" package of R. The differential gene expression heatmap was generated using the "heatmap" package, and the differential gene

volcano plot was created using the "ggplot2" package. GO and KEGG enrichment analysis was conducted using the "clusterProfiler" package^{61,63}.

DEP consensus clustering analysis

We performed unsupervised consensus clustering analysis using the "ConsensusClusterPlus" R package⁶⁴ to classify samples into different protein subtypes. We set the number of clusters from 2 to 9 and determined the optimal number of clusters based on the following criteria: identifying the inflection point of the Cumulative Distribution Function (CDF) curve where the slope decreases, ensuring that clusters with too few samples were not included, and ensuring high intragroup correlation and low intergroup correlation for the selected clusters. Additionally, DEPs from different protein subtypes were assigned to different protein group subtypes in a similar manner⁶⁵.

Construction of protein-protein interaction network

The protein interaction network was constructed using the STRING tool. We visualized gene interactions using Cytoscape software (V.3.7.2). To identify the most densely connected regions; we utilized the Mcode plugin in Cytoscape and set parameters based on topological principles. The parameter settings we employed were as follows: MCODE score > 5, degree cutoff = 2, node score cutoff = 0.2, max depth = 100, k -score = 2⁶⁶.

We performed protein-protein interaction analysis for DEGs using the STRING database (<http://string-db.org/>) and constructed the protein interaction network with a minimum confidence score > 0.7. The results were further analyzed using the MCODE plugin in Cytoscape to evaluate the network topology and identify core proteins related to HIRI development⁶⁷.

Functional enrichment analysis of DEGs and DEPs

We performed GO and KEGG functional enrichment analysis using the "ClusterProfiler" package in R software. For GO enrichment analysis, we analyzed the biological processes (BP), cellular components (CC), and molecular functions (MF) using $P < 0.05$ as the filtering criteria. Additionally, we visualized the enriched pathways and genes. In the KEGG enrichment analysis, we also used $P < 0.05$ as the significance threshold to visualize the enriched pathways and genes, successfully identifying the differential enrichment of marker genes in different clusters⁶⁸.

ROC curve analysis

We used the "pROC" package in R software to plot a ROC curve and calculate the area under the curve (AUC) value to validate the predictive performance of the identified biomarkers⁶⁹.

Cell culture and transfection

Human normal liver cells (MIHA) (Bio-132746, Microbial Culture Collection, Beijing, China), the mouse hepatocyte line AML12 (CBP60909, Nanjing Cobioer Biotechnology Co., Ltd., Jiangsu, China), and HEK-293T (CBP60661, Nanjing Bioscience & Technology Co., Ltd., Jiangsu, China) were cultured in DMEM medium (11965092, Gibco, USA) containing 10% FBS (TMS-016, Sigma Aldrich, USA), 10 µg/mL gentamicin (85886, Sigma Aldrich, USA), and 100 U/mL penicillin (9073-60-3, Sigma Aldrich, USA). The cells were maintained in a Heracell™ Vios 160i CO₂ incubator (51033770, Thermo Scientific™, Germany) at 37°C with 5% CO₂. Subculture was performed when the cell growth reached 80% to 90% confluence⁷⁰⁻⁷².

In the H/R experiment, MIHA cells and AML12 cells were exposed to 24 h of hypoxia (5% CO₂, 1% O₂, and 94% N₂), followed by 18 h of reoxygenation at 37°C (5% CO₂, 21% O₂, and 74% N₂)⁷³.

Grouping: oe-NC+Lv-NC (transfected with oe-NC and Lv-NC), oe-Stat1 + Lv-NC (transfected with oe-Stat1 and Lv-NC), oe-Stat1 + Lv-miR-497-5p (transfected with oe-Stat1 and Lv-miR-497-5p), sh-NC+In-NC (transfected with sh-NC and In-NC), sh-Stat1 + In-NC (transfected with sh-Stat1 and In-NC), sh-Stat1 + In-miR-497-5p (transfected with sh-Stat1 and In-miR-497-5p), oe-NC+sh-NC (transfected with oe-NC and sh-NC), oe-Stat1+sh-NC (transfected with oe-Stat1 and sh-NC), oe-Stat1+sh-HDAC7 (transfected with oe-Stat1 and sh-HDAC7).

Lentiviruses

Recombinant lentiviral particles and viral packaging reagents were purchased from Sigma-Aldrich (Shanghai, China) for Lv-NC, Lv-*miR-497-5p*, In-NC, In-*miR-497-5p*, oe-NC, oe-*Stat1*, oe-HDAC7, sh-NC, and sh-*Stat1*. HEK-293T cells were co-transfected separately with the packaged viruses and target vectors using Lipofectamine 2000 (Invitrogen, Carlsbad, CA, USA). After 48 h of cell culture, the viral titers were determined using the p24 ELISA assay kit (Cell Biolabs, San Diego, CA, USA), and the viruses were titrated to 10^9 transduction units (TU)/mL. A total of 5×10^5 liver cells were seeded in a six-well plate, and when the cell density reached 70–90%, the cells were transfected with an appropriate amount of packaged lentivirus (MOI = 10, working titer $\sim 5 \times 10^6$ TU/mL) and 5 μ g/mL polybrene (Merck, Darmstadt, Germany) in the culture medium. After 4 h of transfection, an equal volume of culture medium with diluted polybrene was added, and fresh culture medium was replaced after 24 h. After 48 h of transfection, the transfection efficiency was observed using a luciferase reporter gene, and stably transduced cell lines were selected using 10 μ g/mL puromycin (Gibco, Carlsbad, CA, USA). The sequences for gene silencing are shown in Supplementary Table 3⁷⁴.

H&E staining

The steps involved in paraffin sectioning of mouse liver tissues are as follows: Initially, the sections were immersed in xylene I for 10 min, followed by immersion in xylene II for another 10 min. Subsequently, the sections were transferred to absolute ethanol I for 5 min and then to absolute ethanol II for an additional 5 min. Next, the sections were placed in 95% ethanol for 5 min, followed by immersion in 90% ethanol for 5 min. Then, the sections were successively immersed in 80% and 70% ethanol for 5 min each before being washed with distilled water. Once deparaffinization and dehydration were completed, the sections were immersed in Harris hematoxylin solution for 10–30 min, followed by rinsing with tap water. The sections were then exposed to 1% hydrochloric acid alcohol for a few seconds, rinsed with tap water, and subsequently counterstained with 0.6% ammonia water to obtain a blue color. The sections were further rinsed with running water and immersed in Eosin Y solution for 1–3 min. Subsequently, the sections were dehydrated and cleared by immersing them successively in 95% ethanol I, 95% ethanol II, absolute ethanol I, absolute ethanol II, xylene I, and xylene II for 5 min each. After removing the sections from the xylene and allowing them to air dry slightly, they were mounted using a neutral mounting medium. Finally, the morphology of the tissues was observed under an Olympus BX63 microscope (Japan), and the experiments were repeated three times. Five random fields were selected for the analysis of cell morphology and structure. All reagents used in the experiments were purchased from Sangon Biotech Co., Ltd. (Guangzhou, China)⁷⁵.

For the quantitative assessment of HIRI in mice, we utilized the Suzuki score to measure the severity of inflammation and tissue damage. The score ranges from 0 to 4, with higher scores indicating more severe damage^{76,77}. Please refer to Supplementary Table 4 for specific scoring details.

RT-qPCR

When extracting mRNA or miRNA from tissues or cells, we employed the Trizol method for tissue RNA extraction. The detailed protocol for tissue RNA extraction can be found in the manual provided by Thermo Fisher Scientific, New York, USA (Trizol Reagent, 16096020, AM1561). We took 5 μ g of tissue RNA and followed the instructions provided by Takara, Japan (RT-qPCR Kit, RR047A) to perform mRNA reverse transcription into cDNA. The synthesized cDNA was then used in conjunction with the ABI PRISM 7300 RT-PCR system (Applied Biosystems) and Fast SYBR Green PCR master mix (Applied Biosystems, 4309155, USA) for RT-qPCR detection. For miRNA cDNA synthesis, we followed the guidelines of the TaqMan microRNA assay kit (Applied Biosystems, 4440888, USA). In the RT-qPCR reaction, FastStart Universal SYBR Green Master Mix (Merck, FSUSGMMR0, USA) was used, with each well containing three replicates. The reference gene for *miR-497-5p* was U6, while for other genes, β -actin served as the reference gene. To represent the fold change in the expression

of the target gene between the experimental group and the control group, the $2^{-\Delta\Delta Ct}$ formula was utilized. The formula is as follows: $\Delta\Delta Ct = (\text{average Ct value of the target gene in the experimental group} - \text{average Ct value of the reference gene in the experimental group}) - (\text{average Ct value of the target gene in the control group} - \text{average Ct value of the reference gene in the control group})$. Ct represents the number of amplification cycles required for the real-time fluorescence intensity to reach a predetermined threshold, at which point the amplification exhibits exponential growth. The experiment was repeated three times. For primer design, please refer to Supplementary Table 5.

Western blot

Liver cells and liver tissue were collected. The cultured cells and tissue were digested using trypsin (T4799-5G, Sigma-Aldrich, USA) and collected. Cell lysis was performed using enhanced RIPA lysis buffer (AR0108, Wuhan Bode Technology Co., Ltd., Wuhan, China) containing protease inhibitors. The protein concentration was determined using the BCA protein assay kit (AR1189, Wuhan Bode Technology Co., Ltd., Wuhan, China).

SDS-PAGE was performed for protein separation. The separated proteins were transferred to a PVDF membrane. The membrane was blocked with 5% BSA (9048-46-8, Sigma-Aldrich, USA) for 1 h at room temperature. Diluted primary antibodies (see Supplementary Table 6 for detailed information) were added and incubated overnight at 4°C. The membrane was washed three times with TBST (5 min each time). Then, either Anti-Mouse-HRP secondary antibody (7076, 1/5000; CST, USA) or Anti-Rabbit-HRP secondary antibody (7074, 1/5000; CST, USA) was added and incubated for 1 h at room temperature. The membrane was washed three times with TBST (5 min each time). TBST was removed, and an appropriate amount of ECL working solution (Omt-01, Beijing Omnitjet Biotech Co., Ltd., Beijing, China) was added. The membrane was incubated at room temperature for 1 min, excess ECL reagents were removed, and the membrane was sealed with plastic wrap and placed in a dark box. X-ray film exposure, development, and fixing were performed for 5–10 min. The bands in the Western blot images were quantified for their grayscale using Image J analysis software. β -Actin was used as an internal reference^{78,79}. Each experiment was repeated three times. All the uncropped western blot images are provided in the Supplementary information (Supplementary Fig. 14).

CCK-8 assay

Liver cells in the logarithmic growth phase were seeded in 96-well plates at a density of 5×10^3 cells per well. After 24 h of seeding, 10 μ L of CCK-8 assay kit solution (C0038, Beyotime, Shanghai, China) was added to each well. The plate was incubated in a culture incubator at 37°C with suitable humidity. After 1 h of incubation, the absorbance values of each well were recorded at 450 nm using a Microplate Reader (abx700005, Beijing Qiweiycheng Technology Co., Ltd.)⁸⁰.

TUNEL fluorescent staining

For apoptosis analysis, we used the TUNEL assay following the manufacturer's instructions (C1086, Beyotime, Shanghai, China). Briefly, cells were treated with proteinase K and 3% hydrogen peroxide, then incubated with the TUNEL reaction mixture in a humid chamber at 37°C. Cell fixation was performed with the immunostaining fixing solution (P0098, Beyotime, Shanghai, China) from Biotek for 30 min. For tissue samples, we added proteinase K (ST532/ST533, Beyotime, Shanghai, China) at a concentration of 20 μ g/mL without DNase and allowed it to act with the immunostaining washing solution at room temperature for 15–30 min. Next, we added 50 μ L of TUNEL detection solution to the samples and incubated them at 37°C in the dark for 60 min. The samples were then washed three times with PBS and mounted with anti-fade sealing liquid for observation using a fluorescence microscope (Zeiss Observer Z1, Germany). The fluorescence was excited at a wavelength range of 450–500 nm and emitted at a range of 515–565 nm (green fluorescence). The target region was selected in the images for fluorescence intensity measurement, and ImageJ software was used for image processing and quantification of positive cells⁸¹.

Flow cytometry

Cell apoptosis was evaluated by flow cytometry using the Annexin V-FITC apoptosis detection kit (APOAF-20TST, Sigma-Aldrich, USA) according to the manufacturer's instructions. Cells were plated at a density of 4×10^5 cells per well in a 6-well plate and allowed to attach overnight. Then, the cells were treated with different concentrations of Cytarabine (0.125, 0.25, 0.5 μ g/mL) for 48 h. After drug treatment, cells were incubated with 200 μ L of binding buffer and stained with Annexin V-FITC in the dark for 20 min. The cells were analyzed using the FACS Aria II flow cytometer⁸². The cell phenotype in the upper right quadrant represented Annexin V + PI+ cells, indicating late apoptotic cells. The cell phenotype in the lower right quadrant represented Annexin V + PI- cells, indicating early apoptotic cells. The cell phenotype in the upper left quadrant represented Annexin V-PI+ cells, indicating dead cells. The cell phenotype in the lower left quadrant represented Annexin V-PI- cells, indicating live cells⁸³. Flow Cytometry (Facs) Plots are provided in the Supplementary information (Supplementary Fig. 15).

TEM

Cells were harvested and fixed with 2.5% glutaraldehyde (111-30-8, Sigma-Aldrich, USA), soaked in darkness for 1 h, and post-treated with 4% formaldehyde (50-00-0, Sigma-Aldrich, USA). Next, cell dehydration was performed using increasing concentrations of acetone (48358, Sigma-Aldrich, USA), followed by embedding the cells in epoxy resin (1675-54-3, Sigma-Aldrich, USA). The cells were polymerized by placing them in an oven at 42°C for 2 h, followed by overnight incubation at 52°C and another overnight incubation at 62°C. Ultra-thin sections of 50–70 nm were prepared using a Leica Biosystems EM UC6 ultramicrotome (Germany). The sections were briefly treated with a 1% uranyl acetate (XHL2375, Hubei Xinhongli Chemical Co., Ltd., China) aqueous solution for 5 min and then placed in a CO₂-free environment for 2–4 min to generate citrate. The sections were observed under a 100 kV Hitachi H7650 transmission electron microscope (DOLEE), and the images were digitally captured using an AMT V700 side-mounted camera⁸⁴.

Immunofluorescence staining

Glass slides with cells were fixed in 4% PFA (G2130, Solarbio, Beijing, China) for 30 min, permeabilized, and then blocked with 0.3% Triton X-100 (T8200, Solarbio, Beijing, China) combined with 5% BSA (SA8130, Solarbio, Beijing, China) for 1 h. The blocking solution was replaced with a mixture of rabbit anti-*Stat1* (K002420P, solarbio, Beijing, China) diluted 1:500 and rabbit anti-HNF4 (ab92378, Abcam, UK) diluted 1:200 in the blocking solution. These primary antibodies were incubated overnight at 4°C. The secondary antibody mixture consisted of goat anti-rabbit IgG conjugated with Alexa Fluor® 488 (ab150077, Abcam, UK) diluted 1:1000 and goat anti-rabbit IgG conjugated with Alexa Fluor® 647 (ab6940, Abcam, UK). After incubation at room temperature for 1 h, DAPI staining was performed. Finally, the slides or tissue sections were washed three times in PBS. Images were captured using a Carl Zeiss AG confocal laser scanning microscope (CLS M; LSM 510 META). Five random fields were selected for analysis, and ImageJ software was used to quantify the number of fluorescent signal-emitting cells (positive cells) and the total number of cells stained with DAPI in each field. The percentage of positive cells was calculated as (number of positive cells/total number of cells) $\times 100\%$ ^{85,86}.

Detection of total ROS and mitochondrial ROS

To detect ROS, we utilized the fluorescent dye 2',7'-dichlorodihydro-fluorescein diacetate (DCFDA) (HY-D0940, Abcam, UK), which enters cells and forms a green fluorescent compound upon interaction with active oxygen molecules. In brief, a stock solution of DCFDA (10 mM) was prepared in methanol and further diluted with culture medium to a working solution of 100 μ M. Hepatocytes (2×10^4) were seeded in wells of a six-well plate on coverslips overnight. On the following day, the cells were treated with H₂O₂ (200 μ M) for 24 h. After treatment, coverslips were washed with ice-cold Hank's balanced salt solution (HBSS) (H8264, Sigma Aldrich, Shanghai, China) and incubated with 100 μ M DCFDA at 37°C for 30 min. After

washing with 1 \times PBS, the coverslips were mounted on glass slides. The images were analyzed using a Nikon A1R multiphoton confocal microscope with a $\times 100$ objective lens and Nikon Imaging Software (NIS Element). Mitochondrial superoxide compounds (SOX) were evaluated using the red compound mito-SOX (M36008, Thermo Fisher, USA). Hepatocytes (2×10^4) were seeded on coverslips placed in wells of an inserted six-well plate overnight. On the following day, the cells were treated with H₂O₂ (200 μ M) for 24 h. The coverslips were then washed with ice-cold 1 \times PBS and incubated with a working solution of 2 μ M mito-SOX at 37°C for 30 min. After washing with 1 \times PBS, the coverslips were mounted on glass slides. Images were obtained using a multiphoton confocal microscope with a $\times 100$ objective lens and analyzed using Nikon Imaging Software (NIS Element)⁸⁷.

Biochemical analysis

Serum or cellular lipid levels were measured using an automated standardized procedure (Roche Hitachi 917/747, Mannheim, Germany) for the following markers: AST, ALT, MDA, GSH, and SOD⁸⁸.

Enzyme-linked immunosorbent assay (ELISA)

The expression of IL-1 β (ab197742-mouse, ab214025-human, Abcam, UK) and IL-6 (ab222503-mouse, ab178013-human, Abcam, UK) in mouse serum and liver cell MIHA supernatant was detected using ELISA kits (Abcam, USA). The assay was performed according to the instructions provided in the kit: 0.1 mL of serum or cell supernatant was added to the wells of a 96-well plate, followed by incubation at 37°C for 1 h. The plate was then washed (blank wells were also washed), and after drying slightly, the wash buffer was discarded. Freshly diluted enzyme-conjugated antibody (at the appropriate dilution determined by titration) was added to each well (0.1 mL) and incubated at 37°C for 0.5–1 h. After washing and drying, the wash buffer was discarded. TMB substrate solution (0.1 mL) was added to each well and incubated at 37°C for 10–30 min. Finally, the absorbance (OD) of each well was measured using an enzyme-linked immunosorbent assay reader, and the concentrations of TNF- α , IL-1 β , and IL-6 were calculated^{89,90}. Each experiment was repeated three times.

Chromatin immunoprecipitation (ChIP)

To assess the binding of *Stat1* to the *miR-497-5p* promoter region, we performed chromatin immunoprecipitation experiments using the EZ-Magna ChIP TMA Kit (17-10086, Merck, USA). First, logarithmic growth phase HEK-293T cells from different groups were cross-linked with 1% formaldehyde for 10 min, followed by quenching with 125 mM glycine at room temperature for 5 min. Next, the cells were washed twice with pre-chilled PBS and collected by centrifugation at 2000 rpm for 5 min. The cells were then resuspended in cell lysis buffer containing 150 mM NaCl, 50 mM Tris (pH 7.5), 5 mM EDTA, 0.005% NP40, and 0.01% Triton X-100, resulting in a cell concentration of 2×10^6 cells per 200 mL. A proteinase inhibitor mixture was added, followed by centrifugation at 5000 rpm for 5 min and resuspension in nuclear lysis buffer. The solution was then sonicated in an ice water bath for 10 min until chromatin fragments of 200–1000 bp were obtained. After centrifugation at 14000 g for 10 min at 4°C, the supernatant was collected. For each group, 100 μ L of the supernatant (DNA fragments) was taken and mixed with 900 μ L of ChIP dilution buffer and 20 μ L of 50 \times PIC. Each group was then added with 60 μ L of Protein A Agarose/Salmon Sperm DNA. The mixture was gently rotated at 4 °C for 1 h, followed by incubation at 4 °C for 10 min and centrifugation at 700 rpm for 1 min. The supernatant was collected, with 20 μ L reserved as Input. In the experimental group, the supernatant was mixed with 1 μ L of *Stat1* (ab234400, rabbit source, Abcam, UK), while in the negative control group, 1 μ L of rabbit IgG (ab172730, Abcam, UK) was added. Each group was then added with 60 μ L of Protein A Agarose/Salmon Sperm DNA and rotated at 4°C for 2 h. After 10 min of incubation at room temperature, the mixture was centrifuged at 700 rpm for 1 min. The supernatant was removed, and the precipitate was washed with low salt buffer, high salt buffer, LiCl solution, and TE solution (twice). Each wash used 250 mL of ChIP wash buffer. Cross-linking was reversed by adding 20 mL of 5 M NaCl, and the DNA was

recovered after the completion of cross-linking. The promoter region of *miR-497-5p* in the complex was quantified using fluorescence quantitative PCR with primers F: 5'-GCGCAGCAGCACACTGTG-3' and R: 5'-GTGCAGGGTCCGAGGT-3⁹¹.

Dual-luciferase reporter gene assay experiment

To verify the transcriptional regulation of *miR-497-5p* by *Stat1*, we followed the instructions of the Promega Dual-Luciferase Reporter Assay System. First, we cloned the cDNA containing the promoter region sequence of *miR-497-5p* into the pGL3-basic luciferase reporter gene vector (GeneCreate, China), obtaining the pGL3-*miR-497-5p* plasmid. Simultaneously, we constructed the *Stat1* overexpression vector. Then, HEK-293T cells were seeded in six-well plates at a density of 2×10^5 cells per well. After cell attachment, oe-*Stat1* and pmirGLO-*miR-497-5p*-WT/pmirGLO-*miR-497-5p*-MUT were co-transfected into HEK-293T cells using Lipofectamine 2000 (11668019, Invitrogen, CA, USA). Forty-eight hours post-transfection, the cells were lysed, and the supernatant was collected after centrifugation at 12,000 g for 1 min. Next, the Dual-Luciferase Reporter Gene Assay System (E1910, Promega) was used to measure luciferase activity. Each cell sample was added with 100 μ L of the Firefly luciferase working solution to measure Firefly luciferase activity and 100 μ L of the Renilla luciferase working solution to measure Renilla luciferase activity. The ratio of Firefly luciferase to Renilla luciferase was calculated as the relative luciferase activity. To validate the targeting relationship between *miR-497-5p* and HDAC7, we artificially synthesized a gene fragment of HDAC7 3'UTR and designed seed sequence complementary site mutations on the wild-type HDAC7. WT and MUT were co-transfected with miR-96-5p into HEK-293T cells, and each experiment was repeated three times⁹². Subsequent experiments were performed in the same manner, and each experiment was repeated three times.

Statistics and Reproducibility

All data were processed using GraphPad Prism 9.0. Quantitative data are presented as mean \pm standard deviation (Mean \pm SD). Unpaired *t*-test was used for comparisons between two groups, while one-way analysis of variance (ANOVA) and Tukey's post hoc multiple comparison test were used for comparisons between multiple groups. Data analysis was performed using one-way analysis of variance and Student's *t*-test. In all graphs and charts, * denotes $P < 0.05$, ** $P < 0.01$, and *** $P < 0.001$, indicating statistical significance⁵³.

Ethics approval and consent to participate

The experimental protocol and animal usage plan have been approved by The First Affiliated Hospital of Xinjiang Medical University's Animal Ethics Committee (Approval No: A230307-81) and the Institutional Animal Care and Use Committee of the Affiliated Huai'an No.1 People's Hospital of Nanjing Medical University.

Reporting summary

Further information on research design is available in the Nature Portfolio Reporting Summary linked to this article.

Data availability

The sequencing data generated in this study have been deposited in the NCBI Sequence Read Archive (SRA) under BioProject accession number PRJNA1304678. The SRA accession IDs are SRR34954865, SRR34954864, SRR34954853, SRR34954842, SRR34954841, SRR34954840, SRR34954839, SRR34954838, SRR34954837, SRR34954836, SRR34954863, SRR34954862, SRR34954861, SRR34954860, SRR34954859 (control group) and SRR34954858, SRR34954857, SRR34954856, SRR34954855, SRR34954854, SRR34954852, SRR34954851, SRR34954850, SRR34954849, SRR34954848, SRR34954847, SRR34954846, SRR34954845, SRR34954844, SRR34954843 (case group). The proteomics datasets are available in the iProX repository under accession number [IPX0012976000](https://doi.org/10.1186/IPX0012976000) and in the ProteomeXchange Consortium via the PRIDE partner repository with the dataset identifier [PXD067240](https://doi.org/10.6065/PX/067240). Uncropped and unedited blot/gel images (Supplementary

Fig. 14) and All flow cytometry (FACS) plots (Supplementary Fig. 15) are provided in the Supplementary Information. Further requests are available from the corresponding authors upon reasonable request.

Received: 13 January 2025; Accepted: 3 October 2025;

Published online: 10 November 2025

References

- Pan, Q., Luo, Y., Xia, Q. & He, K. Ferroptosis and liver fibrosis. *Int J. Med. Sci.* **18**, 3361–3366 (2021).
- Hirao, H., Nakamura, K. & Kupiec-Weglinski, J. W. Liver ischaemia-reperfusion injury: a new understanding of the role of innate immunity. *Nat. Rev. Gastroenterol. Hepatol.* **19**, 239–256 (2021).
- Guo, J. et al. Hepatocyte-specific TMEM16A deficiency alleviates hepatic ischemia/reperfusion injury via suppressing GPX4-mediated ferroptosis. *Cell Death Dis.* **13**, 1072 (2022).
- Hu, C., Zhao, L., Zhang, F., Li, L. Melatonin and its protective role in attenuating warm or cold hepatic ischaemia/reperfusion injury. *Cell Proliferation* **54**, e13021 (2021).
- Rosa, A. D. Pre-treatment with pregabalin reduces liver ischemia-reperfusion injury in rats: tissue protection with an analgesic. *Eur Rev.* **27**, 10322–10333 (2023).
- Li, R. et al. The gut microbial metabolite, 3,4-dihydroxyphenylpropionic acid, alleviates hepatic ischemia/reperfusion injury via mitigation of macrophage pro-inflammatory activity in mice. *Acta Pharmacologica Sin.* **B 12**, 182–196 (2022).
- Jia, K. et al. Acteoside ameliorates hepatic ischemia-reperfusion injury via reversing the senescent fate of liver sinusoidal endothelial cells and restoring compromised sinusoidal networks. *Int J. Biol. Sci.* **19**, 4967–4988 (2023).
- Zou, S. et al. Mu-opioid receptor alleviated ferroptosis in hepatic ischemia-reperfusion injury via the HIF-1 α /KCNQ1OT1 axis. *Am. J. Physiol. Cell Physiol.* **324**, C927–C940 (2023).
- Luo, N., Yang, C., Zhu, Y., Chen, Q. & Zhang, B. Diosmetin ameliorates nonalcoholic steatohepatitis through modulating lipogenesis and inflammatory response in a STAT1/CXCL10-dependent manner. *J. Agric. Food Chem.* **69**, 655–667 (2021).
- Mao, B., Yuan, W., Wu, F., Yan, Y., Wang, B. Autophagy in hepatic ischemia-reperfusion injury. *Cell Death Discov.* **9**, 115 (2023).
- Jiménez-Castro, M. B., Cornide-Petronio, M. E., Gracia-Sancho, J. & Peralta, C. Inflammasome-mediated inflammation in liver ischemia-reperfusion injury. *Cells* **8**, 1131 (2019).
- Zhu, Y. et al. Involvement of MST1/mTORC1/STAT1 activity in the regulation of B-cell receptor signalling by chemokine receptor 2. *Clin. Transl. Med.* **12**, e887 (2022).
- Yao, X. et al. Dual analysis of wild-type and attenuated Orf virus and host cell transcriptomes revealed novel virus-host cell interactions. *mSphere* **8**, e003982 (2023).
- Luo, J. et al. PIAS1 alleviates hepatic ischemia-reperfusion injury in mice through a mechanism involving NFATc1 SUMOylation. *Dis. Markers* **2022**, 1–22 (2022).
- Christou, C. D. & Tsoulfas, G. The role of microRNA in hepatic ischemia-reperfusion injury. *MiRNA* **9**, 248–254 (2021).
- Zhu, S. F., Yuan, W., Du, Y. L. & Wang, B. L. Research progress of lncRNA and miRNA in hepatic ischemia-reperfusion injury. *Hepatobiliary Pancreat. Dis. Int.* **22**, 45–53 (2023).
- Shao, J. L., Wang, L. J., Xiao, J. & Yang, J. F. Non-coding RNAs: The potential biomarker or therapeutic target in hepatic ischemia-reperfusion injury. *World J. Gastroenterol.* **29**, 4927–4941 (2023).
- Hu, Z. Q. et al. MicroRNAs and long non-coding RNAs in liver surgery: diagnostic and therapeutic merits. *Hepatobiliary Pancreat. Dis. Int.* **19**, 218–228 (2020).
- Dai, Y., Guo, M., Jiang, L. & Gao, J. Network pharmacology-based identification of miRNA expression of *Astragalus membranaceus* in the treatment of diabetic nephropathy. *Medicine* **101**, e28747 (2022).

20. Dervovic, D. et al. In vivo CRISPR screens reveal Serpinb9 and Adam2 as regulators of immune therapy response in lung cancer. *Nat. Commun.* **14**, 3150 (2023).

21. Wang, H. et al. Subtyping of microsatellite stability colorectal cancer reveals guanylate binding protein 2 (GBP2) as a potential immunotherapeutic target. *J. Immunother. Cancer* **10**, e004302 (2022).

22. Wang, J. et al. Integrated analysis of single-cell and bulk RNA sequencing reveals pro-fibrotic PLA2G7high macrophages in pulmonary fibrosis. *Pharmacol. Res.* **182**, 106286 (2022).

23. Qian, Y., Liu, Z. & Geng, X. Lack of protection of ischaemic preconditioning in the rat model of major hepatectomy with ischaemia reperfusion injury. *Asian J. Surg.* **31**, 140–147 (2008).

24. Meng, C., Guo, L. bin, Liu, X., Chang, Y. H. & Lin, Y. Targeting STAT1 in both cancer and insulin resistance diseases. *CPPS* **18**, 181–188 (2016).

25. Ihle, J. N. The Stat family in cytokine signaling. *Curr. Opin. Cell Biol.* **13**, 211–217 (2001).

26. Xu, L. et al. Sevoflurane postconditioning attenuates hepatic ischemia-reperfusion injury by limiting HMGB1/TLR4/NF- κ B pathway via modulating microRNA-142 in vivo and in vitro. *Front Pharmacol.* **12**, 646307 (2021).

27. Lin, C. C. et al. Regulation rewiring analysis reveals mutual regulation between STAT1 and miR-155-5p in tumor immunosurveillance in seven major cancers. *Sci. Rep.* **5**, 12063 (2015).

28. Kohanbash, G. & Okada, H. MicroRNAs and STAT interplay. *Semin. Cancer Biol.* **22**, 70–75 (2012).

29. Ingram, H., Dogan, M., Eason, J., Kuscu, C. & Kuscu, C. MicroRNAs: Novel targets in hepatic ischemia–reperfusion injury. *Biomedicines* **10**, 791 (2022).

30. Wu, K. et al. Downregulation of miR-497-5p prevents liver ischemia-reperfusion injury in association with MED1/TIMP-2 axis and the NF- κ B pathway. *FASEB J.* **35**, e21180 (2021).

31. Menon, P. R., Staab, J., Gregus, A., Wirths, O., Meyer, T. An inhibitory effect on the nuclear accumulation of phospho-STAT1 by its unphosphorylated form. *Cell Commun. Signal.* **20**, 42 (2022).

32. Reich, N. C. & Liu, L. Tracking STAT nuclear traffic. *Nat. Rev. Immunol.* **6**, 602–612 (2006).

33. Mei, J. et al. OIP5-AS1 modulates epigenetic regulator HDAC7 to enhance non-small cell lung cancer metastasis via miR-140-5p. *Oncol Lett.* **20**, 7 (2020).

34. Freese, K. et al. Histone deacetylase expressions in hepatocellular carcinoma and functional effects of histone deacetylase inhibitors on liver cancer cells in vitro. *Cancers* **11**, 1587 (2019).

35. Yamada, N. et al. Iron overload as a risk factor for hepatic ischemia-reperfusion injury in liver transplantation: Potential role of ferroptosis. *Am. J. Transplant.* **20**, 1606–1618 (2020).

36. Bow, Y. D. et al. A novel quinoline derivative, DFIQ, sensitizes NSCLC cells to ferroptosis by promoting oxidative stress accompanied by autophagic dysfunction and mitochondrial damage. *Cancer Cell Int.* **23**, 171 (2023).

37. He, Z. et al. Gut microbiota regulates circadian oscillation in hepatic ischemia–reperfusion injury-induced cognitive impairment by interfering with hippocampal lipid metabolism in mice. *Hepatol. Int.* **17**, 1645–1658 (2023).

38. Malý, O. et al. Inhalation of molecular hydrogen prevents ischemia–reperfusion liver damage during major liver resection. *Ann. Transl. Med.* **7**, 774–774 (2019).

39. Wendisch, D. et al. SARS-CoV-2 infection triggers profibrotic macrophage responses and lung fibrosis. *Cell* **184**, 6243–6261.e27 (2021).

40. Liao, C. & Beisel, C. L. The tracrRNA in CRISPR biology and technologies. *Annu Rev. Genet.* **55**, 161–181 (2021).

41. Westermann, A. J. & Vogel, J. Cross-species RNA-seq for deciphering host–microbe interactions. *Nat. Rev. Genet.* **22**, 361–378 (2021).

42. Li, J., Jin, C., Li, Y., Liu, H. Mid1 aggravates hepatic ischemia–reperfusion injury by inducing immune cell infiltration. *FASEB J.* **38**, e23823 (2024).

43. Li, H. et al. Pectolinarigenin attenuates hepatic ischemia/reperfusion injury via activation of the PI3K/AKT/Nrf2 signaling pathway. *Chem. Biol. Interact.* **386**, 110763 (2023).

44. Huang, Z. et al. Inhibition of miR-450b-5p ameliorates hepatic ischemia/reperfusion injury via targeting CRYAB. *Cell Death Dis.* **11**, 455 (2020).

45. Huang, Z. et al. MicroRNA-125b protects liver from ischemia/reperfusion injury via inhibiting TRAF6 and NF- κ B pathway. *Biosci. Biotechnol. Biochem.* **83**, 829–835 (2019).

46. Jin, X. et al. Unveiling circular RNA-mediated regulatory mechanisms in necroptosis in premature ovarian failure. *Front. Biosci. (Landmark Ed.)* **28**, 314 (2023).

47. Lu, W. et al. Comprehensive analysis of HDAC7 expression and its prognostic value in diffuse large B cell lymphoma: A review. *Medicine* **102**, e34577 (2023).

48. Wang, Y. et al. Histone deacetylase 7: a signalling hub controlling development, inflammation, metabolism and disease. *FEBS J.* **290**, 2805–2832 (2022).

49. Li, T. T. et al. FBXW5 aggravates hepatic ischemia/reperfusion injury via promoting phosphorylation of ASK1 in a TRAF6-dependent manner. *Int. Immunopharmacol.* **99**, 107928 (2021).

50. Li, J. et al. Epoxidation catalyzed by the nonheme iron(ii)- and 2-oxoglutarate-dependent oxygenase, asqj: mechanistic elucidation of oxygen atom transfer by a ferryl intermediate. *J. Am. Chem. Soc.* **142**, 6268–6284 (2020).

51. Hu, Q. Z. et al. HSP110 aggravates ischemia–reperfusion injury after liver transplantation by promoting NF- κ B pathway. *Hepatobiliary Pancreat. Dis. Int.* **23**, 344–352 (2024).

52. PRINGLE, J. H. Notes on the arrest of hepatic hemorrhage due to trauma. *Ann. Surg.* **48**, 541–549 (1908).

53. Liu, Y. et al. Activation of YAP attenuates hepatic damage and fibrosis in liver ischemia–reperfusion injury. *J. Hepatol.* **71**, 719–730 (2019).

54. Liu, Z. Z. et al. Autophagy receptor OPTN (optineurin) regulates mesenchymal stem cell fate and bone–fat balance during aging by clearing FABP3. *Autophagy* **17**, 2766–2782 (2020).

55. Arunachalam, D. et al. Expression of immune response genes in human corneal epithelial cells interacting with *Aspergillus flavus* conidia. *BMC Genomics* **23**, 5 (2022).

56. Linkner, T. R. et al. Cellular proteo-transcriptomic changes in the immediate early-phase of lentiviral transduction. *Microorganisms* **9**, 2207 (2021).

57. Deng, Y. J. et al. GRB10 and E2F3 as diagnostic markers of osteoarthritis and their correlation with immune infiltration. *Diagnostics* **10**, 171 (2020).

58. Yu, B. et al. Diagnostic and predictive value of immune-related genes in Crohn's disease. *Front. Immunol.* **12**, 643036 (2021).

59. Xie, J., Yang, P., Wei, H., Mai, P. & Yu, X. Development of a prognostic nomogram based on an eight-gene signature for esophageal squamous cell carcinoma by weighted gene co-expression network analysis (WGCNA). *Ann. Transl. Med.* **10**, 88–88 (2022).

60. Jianping, W. et al. Identifying DUSP-1 and FOSB as hub genes in immunoglobulin A nephropathy by WGCNA and DEG screening and validation. *PeerJ* **10**, e13725 (2022).

61. Guo, H. et al. Dynamic TMT-based quantitative proteomics analysis of critical initiation process of totipotency during cotton somatic embryogenesis transdifferentiation. *IJMS* **20**, 1691 (2019).

62. Wang, Z. et al. Plasma proteome profiling of high-altitude polycythemia using TMT-based quantitative proteomics approach. *J. Proteom.* **194**, 60–69 (2019).

63. Friedrich, C. et al. Comprehensive micro-scaled proteome and phosphoproteome characterization of archived retrospective cancer repositories. *Nat. Commun.* **12**, 3576 (2021).

64. Wilkerson, M. D. & Hayes, D. N. ConsensusClusterPlus: a class discovery tool with confidence assessments and item tracking. *Bioinformatics* **26**, 1572–1573 (2010).

65. Zhang, Y., Chen, F., Chandrashekhar, D. S., Varambally, S., Creighton, C. J. Proteogenomic characterization of 2002 human cancers reveals pan-cancer molecular subtypes and associated pathways. *Nat Commun.* **23**, 794 (2022).

66. Xie, R., Li, B., Jia, L. & Li, Y. Identification of Core Genes and Pathways in Melanoma Metastasis via Bioinformatics Analysis. *IJMS* **23**, 794 (2022).

67. Mering, C. v. STRING: a database of predicted functional associations between proteins. *Nucleic Acids Res.* **31**, 258–261 (2003).

68. Lin, R. et al. Identification of ferroptosis genes in immune infiltration and prognosis in thyroid papillary carcinoma using network analysis. *BMC Genomics.* **22**, 576 (2021).

69. Jiang, L. et al. Exploring diagnostic m6A regulators in endometriosis. *Aging* **12**, 25916–25938 (2020).

70. Lyu, Z. J. et al. Recurrent ZNF83-E293V mutation promotes bladder cancer progression through the NF- κ B pathway via transcriptional dysregulation of S100A8. *Mol. Ther.* **29**, 275–290 (2021).

71. Zhu, S. et al. Preclinical models for bladder cancer research. *Hematol./Oncol. Clin. North Am.* **35**, 613–632 (2021).

72. Zhang, X., Zhao, Y., Kong, P., Han, M. & Li, B. Expression of circZNF609 is down-regulated in colorectal cancer tissue and promotes apoptosis in colorectal cancer cells by upregulating p53. *Med Sci. Monit.* **25**, 5977–5985 (2019).

73. Wang, M. et al. Methyl eugenol attenuates liver ischemia reperfusion injury via activating PI3K/Akt signaling. *Int. Immunopharmacol.* **99**, 108023 (2021).

74. Yan, R. et al. Knockdown of augmente of liver regeneration in HK-2 cells inhibits inflammation response via the mitogen-activated protein kinase signaling pathway. *Inflamm. Res.* **64**, 453–462 (2015).

75. Yang, M., Chen, C., Wang, K., Chen, Y. & Xia, J. Astilbin influences the progression of osteoarthritis in rats by down-regulation of PGE-2 expression via the NF- κ B pathway. *Ann. Transl. Med.* **8**, 766–766 (2020).

76. Suzuki, S., Toledo-Pereyra, L. H., Rodriguez, F. J. & Cejalvo, D. Neutrophil infiltration as an important factor in liver ischemia and reperfusion injury. Modulating effects of FK506 and cyclosporine. *Transplantation* **55**, 1265–1271 (1993).

77. Zhang, K., Xu, X. & Hu, L. Sevoflurane attenuates hepatic ischemia reperfusion injury by the miR-122/Nrf2 pathway. *Ann. Transl. Med.* **10**, 350–350 (2022).

78. Luo, A. et al. Exosome-derived miR-339-5p mediates radiosensitivity by targeting Cdc25A in locally advanced esophageal squamous cell carcinoma. *Oncogene* **38**, 4990–5006 (2019).

79. Lu, J. et al. Exosomal miR-9 inhibits angiogenesis by targeting MDK and regulating PDK/AKT pathway in nasopharyngeal carcinoma. *J. Exp. Clin. Cancer Res.* **37**, 147 (2018).

80. Chen, L. et al. A necroptosis related prognostic model of pancreatic cancer based on single cell sequencing analysis and transcriptome analysis. *Front Immunol.* **13**, 1022420 (2022).

81. Su, Y. et al. Mutual promotion of apoptosis and autophagy in prepubertal rat testes induced by joint exposure of bisphenol A and nonylphenol. *Environ. Pollut.* **243**, 693–702 (2018).

82. Zhang, T. et al. E2F1-mediated AUF1 upregulation promotes HCC development and enhances drug resistance via stabilization of AKR1B10. *Cancer Sci.* **113**, 1154–1167 (2022).

83. Zhou, K. X. et al. Increased Nuclear Transporter KPNA2 Contributes to Tumor Immune Evasion by Enhancing PD-L1 Expression in PDAC. *J. Immunol. Res.* **2021**, 1–13 (2021).

84. Sui, M. et al. CIRBP promotes ferroptosis by interacting with ELAVL1 and activating ferritinophagy during renal ischaemia-reperfusion injury. *J. Cell. Mol. Med.* **25**, 6203–6216 (2021).

85. Chen, G. et al. Transplanting neurofibromatosis-1 gene knockout neural stem cells improve functional recovery in rats with spinal cord injury by enhancing the mTORC2 pathway. *Exp. Mol. Med.* **54**, 1766–1777 (2022).

86. Li, W., Zhang, S., Liu, J., Liu, Y., Liang, Q. Vitamin K2 stimulates Mc3T3-E1 osteoblast differentiation and mineralization through autophagy induction. *Mol. Med. Rep.* **19**, 3676–3684 (2019).

87. Maity, J. et al. Ferutinin induces osteoblast differentiation of DPSCs via induction of KLF2 and autophagy/mitophagy. *Cell Death Dis.* **13**, 452 (2022).

88. Pan, P. H. et al. Plumbagin ameliorates bile duct ligation-induced cholestatic liver injury in rats. *Biomed. Pharmacother.* **151**, 113133 (2022).

89. Chen, D. et al. Menstrual blood-derived mesenchymal stem cells attenuate inflammation and improve the mortality of acute liver failure combining with A2AR agonist in mice. *J. Gastro Hepatol.* **36**, 2619–2627 (2021).

90. Hu, Q. et al. STING-mediated intestinal barrier dysfunction contributes to lethal sepsis. *EBioMedicine* **41**, 497–508 (2019).

91. Zhang, B. et al. KLF5 activates MicroRNA 200 transcription to maintain epithelial characteristics and prevent induced epithelial-mesenchymal transition in epithelial cells. *Mol. Cell. Biol.* **33**, 4919–4935 (2013).

92. Chen, W. et al. SRC-3 protects intestine from DSS-induced colitis by inhibiting inflammation and promoting goblet cell differentiation through enhancement of KLF4 expression. *Int J. Biol. Sci.* **14**, 2051–2064 (2018).

Acknowledgements

This study was supported by National Natural Science Foundation of China (No. 82360380) and the Xinjiang Uygur Autonomous Region Tianshan Talent Training Program-Leading Talents in Technological Innovation (No.2024T-SYCLJ0047) and the Huai'an Science and Technology Board Natural Science Research Projects (No. HAB202304).

Author contributions

K.W., T.X., and B.J. contributed equally to this work and were responsible for conducting experiments, data collection, and initial manuscript drafting. X.Y.Y., Y.W., and H.S. participated in data analysis, methodology design, and figure preparation. Z.Z. and M.D. assisted with the animal and cell models. S.C.W. contributed to experimental validation and critical revision of the manuscript. L.M. and K.W. conceptualized the study, supervised the research process, and finalized the manuscript. All authors read and approved the final manuscript.

Competing interests

The authors declare no competing interests.

Additional information

Supplementary information The online version contains supplementary material available at <https://doi.org/10.1038/s42003-025-08993-x>.

Correspondence and requests for materials should be addressed to Kun Wu or Long Ma.

Peer review information *Communications Biology* thanks Ma Yong and the other, anonymous, reviewer for their contribution to the peer review of this work. Primary Handling Editor: Dario Ummarino. A peer review file is available.

Reprints and permissions information is available at <http://www.nature.com/reprints>

Publisher's note Springer Nature remains neutral with regard to jurisdictional claims in published maps and institutional affiliations.

Open Access This article is licensed under a Creative Commons Attribution-NonCommercial-NoDerivatives 4.0 International License, which permits any non-commercial use, sharing, distribution and reproduction in any medium or format, as long as you give appropriate credit to the original author(s) and the source, provide a link to the Creative Commons licence, and indicate if you modified the licensed material. You do not have permission under this licence to share adapted material derived from this article or parts of it. The images or other third party material in this article are included in the article's Creative Commons licence, unless indicated otherwise in a credit line to the material. If material is not included in the article's Creative Commons licence and your intended use is not permitted by statutory regulation or exceeds the permitted use, you will need to obtain permission directly from the copyright holder. To view a copy of this licence, visit <http://creativecommons.org/licenses/by-nc-nd/4.0/>.

© The Author(s) 2025